On the Time-Domain Airborne SAR Focusing in the Presence of Strong Azimuth Variations of the Squint Angle

Paolo Berardino, Antonio Natale, Carmen Esposito, Riccardo Lanari, *Fellow, IEEE*, and Stefano Perna, *Senior Member, IEEE*

***Abstract*— Airborne synthetic aperture radar (SAR) data focusing in the presence of highly variable squint angles is addressed in this work. To do this, a time-domain SAR focusing algorithm has been developed to account for the target-dependent nature of the acquisition squint angle. For comparison purposes, we have considered also a SAR processor based on the use of an azimuth-invariant processing squint angle. Moreover, real data acquired by two different X-band airborne SAR systems have been analyzed. The aims of the work are twofold. First, we show that the adoption of an azimuth-invariant processing squint angle, typically pursued by computationally efficient focusing strategies, may become inappropriate in several airborne missions, which are typically corrupted by motion errors induced by atmospheric turbulence. On the contrary, these problems are circumvented through the developed time-domain focusing strategy, which exploits a target-dependent processing squint angle that is coincident with the acquisition one. Second, we show that the proposed focusing strategy must be properly revised in the case of interferometric processing. In particular, we show that if the (target-dependent) acquisition squint angle is different for the two interferometric channels used, we have to move toward a different focusing paradigm, say, an interferometric focusing solution. This is again based on considering a target-dependent processing squint angle, but for each target, this processing angle should be equal neither to the acquisition squint angle of the "main" acquisition nor to that of the "secondary" one: it must instead lie halfway between them. We prove that this approach is appropriate to obtain high interferometric coherence, and it is suboptimal to separately focus the interferometric channels.**

***Index Terms*— Airborne synthetic aperture radar (SAR), back-projection algorithm, squint.**

I. Introduction

As is well known, synthetic aperture radar (SAR) systems [1], [2] can reach high spatial resolution, thanks to the movement of the platform on which they are mounted. In this regard, they can be classified as ground-based SAR systems [3] when arranged on ground track rails, spaceborne SAR systems [4], [5], [6] when mounted on satellites, and aerial SAR systems [7] when installed on airplanes [8], [9], [10], [11], [12], [13], [14], [15], [16], helicopters [17], unmanned aerial vehicles (UAVs) [18], [19], [20], or drones [21]. The use of one of these three different classes of SAR systems, which are complementary in terms of technical capabilities (such as spatial coverage, resolution, and revisit time), impacts the focusing procedure that is adopted to process the raw radar data collected onboard. More specifically, in the ground-based and spaceborne SAR cases, the tracks followed by the platforms are typically very stable, that is, they are locally well approximated as rectilinear ones (at least within the synthetic aperture). Moreover, during the acquisition, the velocity and the attitude (given by the combination of the roll, pitch, and yaw angles) of the platform are practically constant. These particular features make it feasible to apply accurate and computationally efficient SAR data-focusing procedures operating in the spectral domain [1].

In the case of aerial systems, instead, the flight tracks are usually characterized by deviations from an ideal linear trajectory. Furthermore, the platform velocity is not constant during the acquisition, thus producing nonuniform spatial sampling of the raw data along the azimuth direction [1], [2], at least when the radar pulse repetition frequency (PRF) is constant, as is usually the case for common radar systems. Finally, the platform attitude changes during the acquisition, thus inducing variations in the pointing direction of the radar antenna. Therefore, the squint angle [1], [2] becomes dependent also on the slow time. All these effects, related to rather common instabilities of the aerial platforms along the flight track, are referred to as motion errors. Due to the presence of motion errors, the extension to aerial SAR data of the computationally efficient focusing procedures adopted for ground-based or spaceborne SAR data is not straightforward. More specifically, to focus SAR data affected by motion errors, accurate knowledge of the position of the SAR antenna phase center (APC) during the acquisition as well as the topographic profile of the illuminated scene are strictly required [1]. For this reason, the information provided by the navigation unit mounted onboard as well as a digital elevation model (DEM) of the observed area are necessary to focus aerial SAR data. When all these ancillary data are available, the presence of track deviations and forward

Manuscript received 13 February 2023; revised 10 May 2023; accepted 12 June 2023. Date of publication 26 June 2023; date of current version 7 August 2023. This work was supported in part by the 2022–2024 Institute for Electromagnetic Sensing of the Environment of the National Research Council (IREA-CNR) and in part by the Italian Civil Protection Department Agreement. *(Corresponding author: Stefano Perna.)*

Paolo Berardino, Antonio Natale, Carmen Esposito, and Riccardo Lanari are with the Institute for Electromagnetic Sensing of the Environment of the National Research Council (IREA-CNR), Naples, Italy (e-mail: berardino.p@irea.cnr.it; natale.a@irea.cnr.it; esposito.c@irea.cnr.it; lanari.r@irea.cnr.it).

Stefano Perna is with the Dipartimento di Ingegneria (DI), Università degli Studi di Napoli "Parthenope," 80133 Naples, Italy, and also with the Institute for Electromagnetic Sensing of the Environment of the National Research Council (IREA-CNR), 80124 Naples, Italy (e-mail: stefano.perna@uniparthenope.it).

Digital Object Identifier 10.1109/TGRS.2023.3289593

velocity variations can be accounted for in the spectral domain by properly integrating the processing chain tailored to the simpler acquisition geometry characterized by the absence of motion errors. To this aim, the so-called motion compensation (MOCO) steps [22], [23] are added, with the aim of reassigning the SAR data to an ideal linear flight path, named nominal track, with a constant azimuth sampling. Moreover, some additional processing strategies [24], [25], [26] may be implemented with the aim of limiting the effects of the so-called beam-center approximation (BCA) [27], which is necessary to pursue computationally efficient focusing in the spectral domain with integrated MOCO.

We note that the spectral-based approaches with integrated MOCO adopt a nominal linear processing flight path [22], [23], as well as a nominal azimuth-invariant processing Doppler centroid [28].

Regarding the adoption of a nominal linear processing flight path, it can be shown [23] that due to the approximations exploited by such spectral-based focusing approaches with integrated MOCO, the higher the deviations of the actually flown track from the nominal one, the worse the quality of the SAR images obtained.

Adoption of a nominal azimuth-invariant processing Doppler centroid corresponds to the use of a processing squint-angle that is constant along the azimuth direction. However, the attitude fluctuations of the aerial platform during the radar acquisition unavoidably induce, in some flight portions, discrepancies between the actual, say acquisition, squint angle and the processing one, thus impairing, in some areas, the quality of the SAR images.

These effects have been shown in [29], where the performance of a spectral-domain focusing algorithm, namely the extended chirp-scaling one [1] with integrated MOCO [22], have been compared with those of a time-domain focusing approach capable of operating with a space-variant Doppler centroid [29]. In particular, the experiments presented in [29] are relevant to airborne acquisitions intentionally carried out over strongly nonlinear flight paths, specifically, a track involving a drop in altitude of approximately 250 m, a double-bend track, and a track with a 90° curve. From the results presented in [29], it turns out that for these strongly nonlinear acquisition geometries, the spectral-based approaches with integrated MOCO are doomed to fail unless the flown track is subdivided into subtracks, characterized by different nominal tracks and different mean processing Doppler centroids. Moreover, in [29] it is also shown that, at least for the considered strongly nonlinear tracks, the strategy of mosaicking overlapping patches of raw data focused on different nominal grids is suboptimal with respect to the focusing procedures operating in the time domain with a space-variant processing Doppler centroid.

In this work, we present a solution to the problems related to the focusing of airborne SAR data in the presence of strong azimuth variations of the antenna pointing direction, which means strong azimuth variations of the acquisition squint angle. In particular, we deepen the preliminary analysis that we presented in [30] and extend it to the interferometric case. To do this, we have developed a time-domain focusing algorithm that, similar to that in [29], is capable of accounting for the space-variant nature (in both range and azimuth directions) of the squint angle induced by the variations of the pointing direction of the radar antenna during the acquisition. For focusing each target, the algorithm properly selects the corresponding synthetic aperture by using the navigation data collected onboard, to pick the track portion from which the radar antenna illuminates the considered target within its major beam. For comparison purposes, we have also considered a SAR-focusing processor that exploits an azimuth-invariant processing squint angle [28] calculated according to a nominal straight flight track. In particular, to better isolate the effects of the azimuth variations of the squint angle on the obtained SAR image, to design the latter processor, we have pursued a time-domain approach. In this way, we have ruled out some additional image degradation effects potentially related to the other approximations applied by the spectral-based focusing algorithms with integrated MOCO [22], [23]. Both SAR processors have been applied to real data acquired by two different X-band airborne SAR systems.

The aims of the work are twofold. The first one is to show that the adoption of an azimuth-invariant processing squint angle may be inappropriate not only for radar acquisitions intentionally carried out over strongly nonlinear flight paths, as those considered in [29]. To do this, in all the experiments presented, we consider acquisition scenarios representative of a wide class of common aerial SAR missions. They involve flight paths that are planned to be as linear as possible and with no intentionally induced squint angles but are affected by unavoidable motion errors. We show that, in these cases, the adoption of a focusing approach where the target-dependent processing squint angle is equal to the (target-dependent) acquisition one allows us to overcome all the problems arising from the use of an azimuth-invariant processing squint angle.

The second aim is to show that the strategy adopted to obtain accurate focusing in the presence of azimuth variations of the acquisition squint angle may become inappropriate for interferometric purposes; therefore, in this case, the focusing strategy needs to be properly revised as proposed. More specifically, if the (target-dependent) acquisition squint angles of the two interferometric channels[1] are different, focusing the two images with two different (target-dependent) processing squint angles (each of them equal to the corresponding acquisition squint angle) generally leads to an impairment of the coherence of the final interferogram. To circumvent this problem, we show that the two images of the considered interferometric pair must again be focused with a target-dependent processing angle. However, for each target, this processing squint angle must be the same for the main and secondary images and must lie halfway between the different acquisition squint angles of the two interferometric channels. To show this, we consider an airborne dataset acquired through a cross-eyed single-pass interferometric configuration. It is remarked that such a configuration has been not intentionally realized. Indeed, it accidentally occurred during an airborne

[1]In this work, the two channels (as well as the corresponding antennas and/or images) of an interferometric configuration are indicated with the terms "main" and "secondary".

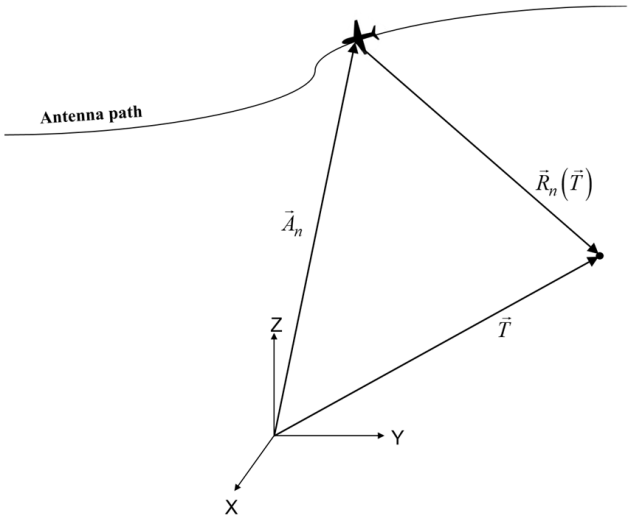

Fig. 1. Airborne SAR acquisition geometry.

SAR mission while mounting a lightweight radar system and the corresponding antennas onboard an aircraft that does not exclusively operate for SAR monitoring purposes. In this regard, it is worth stressing that such an installation scenario is well representative of an increasingly widespread class of aerial SAR missions that involve compact and lightweight systems mounted just before the beginning (and unmounted just after the end) of SAR acquisition campaigns operated through small and flexible aerial platforms [7].

The work is organized as follows. Section II shows the main rationale of the time-domain SAR processor. Section III describes the proposed time-domain focusing procedure based on using a target-dependent processing squint angle capable of accounting for the target-dependent nature of the acquisition one. Section IV shows how the procedure of Section III must be modified to implement a focusing strategy based on the adoption of an azimuth-invariant processing squint angle. In Section V, the two focusing strategies described in Sections III and IV are compared through an experimental analysis conducted on real data acquired by two different X-band airborne SAR systems. Section VI shows how the focusing approach of Section III should be revised in the case of interferometric processing. Section VII reports conclusions and final remarks.

II. SAR Focusing in Time-Domain: Main Rationale

Let us consider the SAR acquisition geometry depicted in Fig. 1: the vector $\vec{A}_n$ represents the position of the radar APC at the (slow) time t_n, whereas the vector $\vec{T}$ represents the position of a generic target to be focused. The vector $\vec{R}_n(\vec{T})$ represents the position of the target with respect to the APC at t_n

$$\vec{R}_n(\vec{T}) = \vec{T} - \vec{A}_n. \tag{1}$$

Its amplitude $R_n(\vec{T}) = |\vec{R}_n(\vec{T})|$ is the antenna-to-target distance at t_n. Let us then consider the so-called *range-focused* SAR signal [1], say $h(n, m)$, obtained by applying a proper processing procedure to the raw radar data recorded onboard. For further details on this processing step aimed at improving the range resolution of the SAR image, the reader can refer to [1]; we just recall that the procedure is very easy to implement and depends on the characteristics of the transmitted waveform [1], [31]. Similar to the raw data, $h(n, m)$ is a 2-D matrix whose indexes $n \in \{1, 2, \ldots, N\}$ and $m \in \{1, 2, \ldots, M\}$ are related to the slow and the fast times, respectively [1], where N and M are the number of recorded azimuth and range samples, respectively.

The focusing procedure, in the time domain, requires that for each target $\vec{T}$, the following coherent summation is carried out[2] [29], [32], [33], [34]:

$$f(\vec{T}) = \sum_{n=k-\frac{K}{2}}^{k+\frac{K}{2}} h(n, m_n) \exp\left[j\frac{4\pi}{\lambda} R_n(\vec{T})\right] w\left[n, R_n(\vec{T})\right] \tag{2}$$

where λ is the wavelength, the index $m_n = m_n[R_n(\vec{T})]$ selects the radar data relevant to the distance $R_n(\vec{T})$ and the weighting function $w(\cdot)$ can account for the attenuation of the received radar echo due to the shape of the antenna pattern as well as the round-trip path of the electromagnetic wave. Moreover, in (2), the indexes K and k define the length (in samples) and the center of the processed synthetic aperture, respectively.

Although the analytical structure of the summation in (2) is quite simple, its implementation requires we apply processing strategies that are peculiar to each specific SAR processor. In particular, to focus the generic target $\vec{T}$ through the implementation of the coherent summation in (2), the following operations must be carried out:

1) calculation of the distance $R_n(\vec{T})$;
2) setting of the length K;
3) evaluation of the index k.

The first two of the above-mentioned steps represent standard procedures that are implemented by all the focusing algorithms tailored to SAR data acquired by aerial platforms. The third step is different in that it is peculiar to each specific SAR processor and is related to the capability of the focusing algorithm to follow the variations of the antenna pointing direction during the radar acquisition.

More specifically, the calculation of the antenna-to-target distance $R_n(\vec{T})$ in (1) is carried out through the use of an available external DEM of the observed area and the flight data recorded by the navigation system, which typically embeds the inertial measurement unit (IMU) and the Global Navigation Satellite System (GNSS). More details relevant to this standard procedure are provided in Appendix A.

The number, K, of samples that define the synthetic aperture length in (2) depends on the required azimuth resolution. Once the latter is fixed, assuming uniform velocity and constant PRF, K depends on the antenna-to-target distance [1]. However, in the presence of track deviations and forward velocity variations, K becomes target-dependent. Therefore, for each considered target, this parameter should be independently set in (2). On the other hand, for flight missions planned to be as rectilinear as possible with a forward velocity as constant as possible, we can safely neglect in (2) the dependence of K from parameters other than the antenna-to-target distance,

[2]In the expression in (2), without any loss of generality, we have considered a monostatic SAR system: extension to the bistatic case can be straightforwardly obtained.

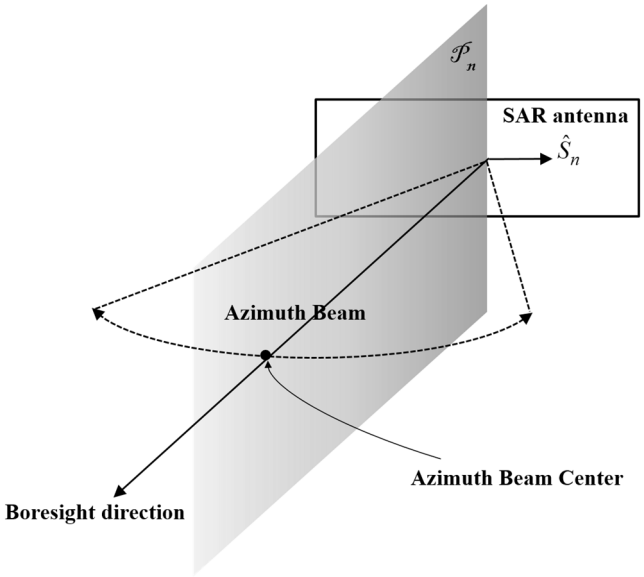

Fig. 2. Relevant to the calculation of the time instant at which the radar antenna illuminates the target at the azimuth beam center: definition of the unit vector $\hat{S}_n$ and the plane $\mathscr{P}_n$.

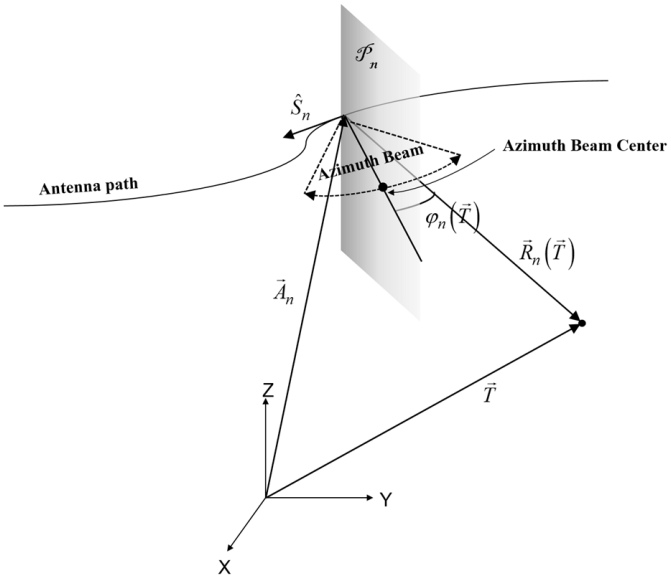

Fig. 3. Relevant to the calculation of the time instant at which the radar antenna illuminates the target at the azimuth beam center: definition of the angle $\varphi_n(\vec{T})$.

thus accepting throughout the focused image very marginal deviations of the obtained azimuth resolution with respect to the set one.

To calculate in (2) the index k that sets the center of the synthetic aperture selected to focus the generic target $\vec{T}$, two different main approaches may be adopted. The first one is capable of accounting for the space-variant nature of the acquisition squint angle induced by the variations of the antenna pointing direction during the radar acquisition. The second one, less accurate but easily compatible with the spectral-based SAR focusing approaches, is based on the use of an azimuth-invariant processing squint angle, computed according to a nominal straight flight track. This approach is, however, not optimal when the acquisition squint angle is azimuth-variant, that is, when the flight path is not rectilinear and the antenna pointing direction changes during the radar acquisition. The two approaches are separately discussed in Sections III and IV.

III. Time-Domain SAR Focusing: Target-Dependent Processing Squint Angle

To account for the azimuth variations of the antenna pointing direction due to the attitude variations of the platform, the index k in (2) must be chosen by finding the time instant t_k at which the radar antenna illuminates the target $\vec{T}$ at the center of the azimuth beam. To do this, let us refer to Fig. 2 where, just for the sake of simplicity and without any loss of generality, we have considered an aperture antenna whose azimuth beam center is at the boresight.[3] In the figure, the unit vector $\hat{S}_n$ is oriented as the azimuth antenna side, whereas the plane $\mathscr{P}_n$, highlighted in gray, is orthogonal to $\hat{S}_n$. Note that for each elevation angle, the direction of the azimuth beam-center lies on the plane $\mathscr{P}_n$. It is remarked that in the presence of attitude variations of the platform, the orientation of the vector $\hat{S}_n$ and the plane $\mathscr{P}_n$ become dependent on the slow time and thus on the index n. To find the time instant t_k at which the target $\vec{T}$ is illuminated by the antenna at its beam center, we have to enforce that $\vec{R}_k(\vec{T})$ belongs to the plane $\mathscr{P}_k$. Accordingly, to find the index k in (2), the following condition must be enforced:

$$\hat{S}_k \cdot \hat{R}_k(\vec{T}) = 0 \tag{3}$$

where $\hat{R}_k(\vec{T})$ is the unit vector associated with the vector $\vec{R}_k(\vec{T})$ defining the direction of the line of sight (LOS) for the target $\vec{T}$ at the (azimuth) beam center, and the operator "$\cdot$" denotes the scalar product. Note that the acquisition squint angle relevant to the target $\vec{T}$ is defined as follows:

$$\Phi(\vec{T}) = \frac{\pi}{2} - \operatorname{acos}\left[\hat{v}_k \cdot \hat{R}_k(\vec{T})\right] \tag{4}$$

where "acos(·)" is the arccosine function and the index k enforces (3). Moreover, $\hat{v}_n$, $n \in \{1, 2, \ldots, N\}$, is the unit vector associated with the platform velocity vector; therefore $\hat{v}_k$ in (4) is the velocity unit vector at the time instant t_k. In (4), we have omitted, for the sake of simplicity, the dependence of the index k on $\vec{T}$. In any case, it is remarked that the acquisition squint angle in (4) is target-dependent. It is also noted that calculating the index k in (2) through the condition in (3) implies that, for each target to be focused, the corresponding synthetic aperture is selected according to a *processing squint angle* that coincides with the actual, target-dependent, acquisition squint angle in (4). For this reason, this case is referred to as focusing with target-dependent processing squint angle.

Numerical calculation of the index k in (2), capable of enforcing the condition in (3), is now in order. To this aim,

[3] A similar procedure can be straightforwardly extended to any other radar antenna whose direction of maximum irradiation is not necessarily at the boresight.

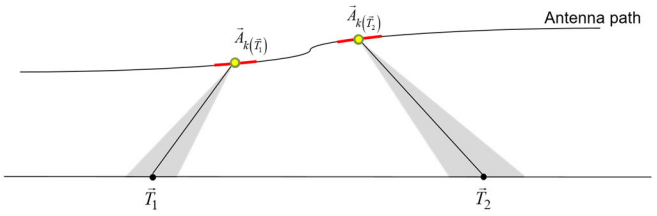

Fig. 4. SAR focusing with a target-dependent processing squint angle. Two targets are considered: $\vec{T}_1$ and $\vec{T}_2$. For each target, the APC position from which the target is illuminated by the radar antenna at the azimuth beam center is represented by a green point. The synthetic aperture used to focus the target is highlighted in red; its center, defined by the index k in (2), is represented by a yellow point. Note that in this case, for each target, the corresponding yellow and green points are coincident.

for a given target $\vec{T}$, we define the following quantity:

$$\varphi_n(\vec{T}) = \frac{\pi}{2} - \text{acos}[\hat{S}_n \cdot \hat{R}_n(\vec{T})], \quad n \in \{1, 2, \ldots, N\} \tag{5}$$

which represents the angular separation between the LOS direction and the plane $\mathscr{P}_n$ (see Fig. 3, where the SAR acquisition geometry is depicted, and Appendix A). Thus, the index k that enforces the condition (3) can be obtained by addressing the following numerical problem:

$$k(\vec{T}) = \underset{n\in\{1,2,\ldots,N\}}{\arg\min} , [|\varphi_n(\vec{T})|] \tag{6}$$

which is a convex one (with the exception of a very limited number of isolated cases occurring in the presence of strongly nonlinear tracks coupled to severe variations of the antenna pointing direction) and it can be effectively solved through local optimization tools. It is finally underlined that to address the optimization problem in (6), we need to calculate the unit vector $\hat{S}_n$ at each time instant t_n. As shown in Appendix B, this can be easily done by following the same rationale adopted to calculate the position $\vec{A}_n$ of the radar APC during the acquisition.

Summing up, SAR focusing with a target-dependent processing squint angle allows following the strong azimuth variations of the acquisition squint angle as depicted in Fig. 4. It can be performed in the time domain by carrying out, for each target, the coherent summation in (2). This basically requires calculating the index k (defining the center of the processed synthetic aperture) following the approach sketched in the block diagram of Fig. 5 (gray box). The inputs are the following:

1) the position of the radar APC with respect to a local reference system defined over the antenna itself (see Appendix B);
2) the antenna lever arm, that is, the position of the radar APC with respect to a local reference system, centered in the IMU phase center, and defined within the aerial vehicle by the IMU itself (see Appendix B);
3) the flight data recorded by the navigation system;
4) an external DEM of the observed area.

Note that the overall procedure shown in Fig. 5 (gray box) basically consists of two subprocedures, highlighted with the light blue and green boxes, respectively. The green box is

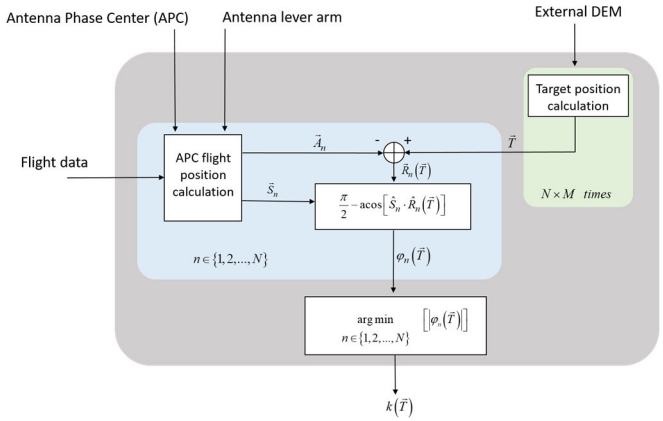

Fig. 5. Block diagram (gray box) of the SAR focusing approach in the time domain with a target-dependent processing squint angle: calculation of the index k in (2). N and M are the number of recorded azimuth and range samples, respectively. The green box is applied for all the $N \times M$ pixels of the SAR image to be focused. For each target extracted within the green box, the light blue box computes N values of all the involved quantities ($\vec{A}_n$, $\vec{S}_n$, $\vec{R}_n$, φ_n).

applied for all the $N \times M$ pixels of the SAR image to be focused. Then, for each target extracted within the green box, the light blue box computes N values of all the involved quantities, namely, the APC flight position $\vec{A}_n$, the antenna vector $\vec{S}_n$, the target to antenna vector $\vec{R}_n$ in (1) and the angle φ_n in (5). For each target, the minimization in (6) (which can be easily addressed through local optimization procedures) leads to the searched index k in (2).

IV. Time-Domain SAR Focusing: Azimuth-Invariant Processing Squint Angle

As remarked before, the calculation of the index k in (2) through enforcement of the condition (3) is a target-dependent procedure, which has to be repeated separately for each target. The calculation of the index k can be carried out through an azimuth-invariant strategy, which is less accurate than the target-dependent one described above. It is underlined that in contrast to the latter strategy, the azimuth-invariant one can be applied by the computationally efficient focusing algorithms that operate in the spectral domain, such as the one proposed in [22], which extends to the airborne case the chirp-scaling approach originally implemented for spaceborne SAR data [1], or the algorithm presented in [35], which extends to the squinted case [28] the zero-squint analysis carried out in [23] for airborne SAR data. For the sake of clearness, in the following, we show how such an azimuth-invariant strategy is applied in the time domain. In this regard, it is worth recalling that the squint angle Φ in (4) becomes independent of the azimuth coordinate of the target when the three following conditions are all enforced (see Appendix C for further details):

1) constant antenna pointing direction during the acquisition (i.e., the orientation of the plane $\mathscr{P}_n$ and the direction of the unit vector $\hat{S}_n$ in Fig. 2 are constant and, therefore, independent of the index n);
2) linear flight path (i.e., the vector $\hat{v}_k$ in (4) is constant and, therefore, independent of the index k);
3) flat topography.

This means that the rigorous computation of the index k in (2) through an azimuth-invariant procedure is appropriate when the three conditions 1)–3) listed above are all enforced. When this does not happen, as in the case of realistic aerial SAR acquisitions, to apply an azimuth-invariant approach for the calculation of the index k in (2) we need to exploit approximated quantities. More specifically, instead of the vector $\vec{S}_n$, we have to consider its average value during the acquisition

$$\vec{S} = \langle \vec{S}_n \rangle \tag{7}$$

where $\langle \cdot \rangle$ is the average operator. Moreover, we have to consider a flat topography (by generating a flat-terrain DEM starting from the available DEM[4]). Finally, following the main rationale of the frequency-domain approaches with integrated MOCO, we have to consider a nominal rectilinear flight path (by setting a proper criterion that allows us to define it starting from the actual flight path) characterized by a constant platform velocity, $\vec{v}$.

By doing so, we can then rewrite (3) and (5) as follows:

$$\hat{S} \cdot \vec{R}_k^{\text{nom}}\left(\vec{T}_{\text{flat}}\right) = 0 \tag{8}$$

and

$$\varphi_n^{\text{nom}}\left(\vec{T}_{\text{flat}}\right) = \frac{\pi}{2} - \text{acos}\left[\hat{S} \cdot \hat{R}_n^{\text{nom}}\left(\vec{T}_{\text{flat}}\right)\right], \quad n \in \{1, 2, \ldots, N\} \tag{9}$$

where $\hat{S}$ is the unit vector associated with $\vec{S}$ and

$$\vec{R}_n^{\text{nom}}\left(\vec{T}_{\text{flat}}\right) = \vec{T}_{\text{flat}} - \vec{A}_n^{\text{nom}}, \quad n \in \{1, 2, \ldots, N\} \tag{10}$$

with $\vec{A}_n^{\text{nom}}$ being the position of the virtual antenna that follows the nominal path (rather than that actually flown), and $\vec{T}_{\text{flat}}$ the position of the target with respect to the flat-terrain DEM. Calculation of the index k in (2) is then obtained by enforcing condition (8). Its numerical evaluation can be addressed by solving the problem in (6), provided that the quantity $\varphi_n(\vec{T})$ is substituted by $\varphi_n^{\text{nom}}(\vec{T}_{\text{flat}})$ in (9), that is,

$$k(\vec{T}) = \underset{n \in \{1,2,\ldots,N\}}{\arg\min} \left[\left|\varphi_n^{\text{nom}}(\vec{T}_{\text{flat}})\right|\right]. \tag{11}$$

We emphasize that calculating the index k in (2) according to the condition in (11) implies that, for each target to be focused, the corresponding synthetic aperture is selected according to the following *processing squint angle*:

$$\Phi_p = \frac{\pi}{2} - \text{acos}\left[\hat{v} \cdot \hat{R}_k^{\text{nom}}\left(\vec{T}_{\text{flat}}\right)\right] \tag{12}$$

which is azimuth-invariant (see Appendix C). For this reason, this case, which is depicted in Fig. 6, is referred to as focusing with an azimuth-invariant processing squint angle. Of course, when the three conditions 1)–3) listed above are not enforced, this procedure becomes suboptimal, since the processing squint angle in (12) becomes different from the actual acquisition squint angle in (4), and the condition of azimuth-invariant squint angle is not valid anymore.

Some additional considerations are now in order.

[4]Note that this does imply the calculation of an average value of the area topography.

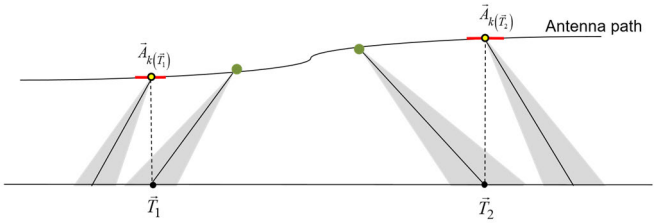

Fig. 6. SAR focusing with an azimuth-invariant processing squint angle. Two equi-range targets are considered: $\vec{T}_1$ and $\vec{T}_2$. For each target, the APC position from which the target is illuminated by the radar antenna at the azimuth beam center is represented by a green point. The azimuth-invariant processing squint angle considered in the figure is equal to zero. The synthetic aperture used to focus the target is highlighted in red; its center, defined by the index k in (2), is represented by a yellow point. Note that in this case, for each target, the corresponding yellow and green points are generally not coincident.

SAR focusing with a significantly azimuth-variant processing squint angle necessarily requires the use of a time-domain approach, as shown in the previous subsection. Differently, SAR focusing with an azimuth-invariant processing squint angle is an approximation peculiar to spectral-based focusing approaches. Notwithstanding, for comparison purposes, we have preferred to apply such an approximation to a time-domain focusing scheme rather than a spectral-based one. The reason is that by doing so we can rule out some additional image degradation effects potentially related to other approximations (such as the independence of the range cell migration effect [1] from the range-variant component of the motion errors [23], or the BCA [27]) that are applied by the spectral-based focusing approaches with integrated MOCO [22], [23]. In this way, we can better isolate the effects occurring in SAR images and/or interferograms that are specifically caused by the use of an azimuth-invariant processing squint angle during the focusing procedure. Summing up, the developed time-domain processor with an azimuth-invariant processing squint angle represents a benchmark for all the frequency-domain approaches with integrated MOCO. Therefore, the comparative results reported in the next sections also provide a useful comparison with the ultimate focusing performance achievable with a generic frequency-domain SAR processor with integrated MOCO.

It is also stressed that to carry out SAR focusing with an azimuth-invariant processing squint angle, we use the flat topography and the nominal rectilinear track only to calculate the index k in (2); the remaining quantities in (2), specifically the distance $R_n(\vec{T})$, are instead calculated by exploiting the available DEM and the actual antenna trajectory along the lines shown in Appendix B.

Furthermore, it is remarked that our work is not intended to provide a strategy for real-time airborne SAR data focusing, which typically tries to take advantage of the computational efficiency of the focusing algorithms rather than their accuracy.

Finally, a short discussion on the computational complexity involved by the time-domain focusing with a target-dependent processing squint angle is now addressed. It is recalled that SAR focusing in the time-domain requires we implement the coherent summation in (2) for each target to focus. The

involved operations that are relevant from the computational point of view are basically two.

First, we need to address the numerical optimization in (6) to find the index k. As observed above, this procedure can be addressed through local approaches. In particular, by referring to "general convex problems" as defined in [36], a loose upper bound for the number of iterations required to reach convergence is on the order of $\log_e(N)$ [36], with $\log_e$ being the natural logarithm and N the number of recorded azimuth samples. As a matter of fact, for common airborne datasets, this upper bound is less than ten.

Second, we need to carry out the $K + 1$ multiplications present in the summation.

When focusing on a whole airborne SAR dataset, the two operations mentioned above must be addressed a number of times that depends on the dimensions of the image. In particular, assuming that the dimensions of the output grid chosen for the focused image are the same as those of the acquired raw data, the optimization problem in (6) as well as the $K + 1$ multiplications in (2) must be executed $N \times M$ times, with M being the number of recorded range samples.

Comparison with the time-domain focusing with azimuth-invariant processing squint angle is finally discussed.

If the used processing squint angle is azimuth-invariant, to focus on a generic target, we still need to carry out the $K + 1$ multiplications present in the summation in (2). When considering the whole airborne SAR dataset, these $K + 1$ multiplications must be executed $N \times M$ times.

Turning to the computation of the index k, with an azimuth-invariant processing squint angle, we need to address the numerical optimization in (11), which is computationally equivalent to that in (6) required in the case of a target-dependent squint angle. When considering the whole airborne SAR dataset, two cases are of interest. If the SAR image is focused in the radar (slant range/azimuth) grid, the numerical optimization in (11) must be addressed only M times, with a not negligible advantage with respect to the target-dependent processing angle approach. On the other hand, if the SAR image is focused on a generic grid not coincident with the radar one (thus taking advantage of the flexibility of the time-domain focusing approaches [29]), the numerical optimization in (11) must be addressed $N \times M$ times, and the overall computational complexity becomes the same as the one of the focusing approach that adopts a target-dependent squint angle.

V. Experiments

In this section, we present some experiments carried out on two different datasets acquired by two different X-band airborne SAR systems, that is, the InSAeS4 [14] and the airborne X-band interferometric SAR (AXIS) [16] sensors, whose main parameters are reported in Tables I and II, respectively. For more extended information on these two systems, the reader is referred to [14] and [16]; here, we just recall that both are equipped with a single-pass interferometric configuration and that InSAeS4 is a pulsed radar whereas AXIS is based on the frequency-modulated continuous wave (FMCW) technology [31]. Moreover, both systems are equipped with the same

Fig. 7. (Left) InSAeS4 system mounted onboard a Learjet 35A. (Right) Airplane (top) along with a zoom (right) on the three radar antennas, which are highlighted with green ellipses.

Fig. 8. (Left) AXIS system mounted onboard a Cessna 172. (Right) The three radar antennas, which are highlighted with green ellipses.

TABLE I
InSAeS4 System Parameters

Radar Parameters	
Radar technology	Pulsed
Peak transmitted power	2600 W
Duty cycle	up to 6%
Carrier frequency	9.55 GHz
Bandwidth	50 – 400 MHz
Pulse Repetition Frequency	0.2 – 16 KHz
Pulse duration	2.6 – 16.2 μs
Recording data rate	up to 32 MB/s
Sampling rate	50 – 400 MHz
Number of range lines	4096
Range resolution (slant)	0.48 – 3.84 m
Antennas	
Number of Tx/Rx Antennas	1
Number of Rx Antennas	2
Polarization	HH
Look-direction	Right

navigation unit, the Applanix POS-AV510, which embeds an IMU and a GNSS to reach high accuracy in the measurement of the position and attitude of the platform during the acquisition, as reported in Table III. In the experiments reported in the following, the InSAeS4 and AXIS systems were mounted onboard a Learjet 35A and a Cessna 172, respectively. Figs. 7 and 8 show the two systems mounted onboard the aircraft. In both figures, the radar antennas are highlighted with green ellipses. It is noted that both systems are equipped with three antennas. In particular, as specified in Tables I and II, InSAeS4 is a multibaseline interferometric system consisting of one transmitting (Tx)/receiving (Rx) antenna and two Rx

TABLE II
AXIS SYSTEM PARAMETERS

Radar Parameters	
Radar technology	FMCW
Transmitted power	5 W
Carrier frequency	9.55 GHz
Bandwidth	200 MHz
Pulse Repetition Frequency	1.2 KHz
Pulse Repetition Interval	833.33 μs
Pulse duration	600.184 μs
Recording data time	605.00 μs
Sampling rate	25 MHz
Number of range lines	7562
Range resolution	0.75 m
Antennas	
Number of Tx Antennas	1
Number of Rx Antennas	2
Polarization	VV
Look-direction	Right

TABLE III
ABSOLUTE ACCURACY SPECIFICATIONS (RMS) OF THE NAVIGATION UNIT*

Position	0.05 m
Velocity	0.005 m/s
Roll & Pitch	0.005°
True Heading	0.008°

*after post-processing integration with GNSS data

antennas [14], whereas AXIS is a single-baseline interferometric system consisting of one Tx and two Rx antennas [16].

The first experiment is relevant to an InSAeS4 dataset acquired in 2013 over an area relevant to Vesuvius volcano, close to the city of Naples (Southern Italy). The acquisition, 15 km long in the azimuth direction, is characterized by very strong attitude variations, which are plotted in Fig. 9. As it can be seen, during the acquisition, the roll varies from $-15°$ to $5°$, the pitch from $4.9°$ to $5.5°$, and the yaw from $-2.5°$ to $-0.5°$. This has led to strong azimuth variations of the squint angle, whose value at midrange is plotted in Fig. 9 and varies from $-7°$ to $1°$ during the acquisition. Especially in the final portion of the track, these variations are particularly severe if compared with the azimuth beamwidth of the two-way antenna pattern, which is $5.6°$. Moreover, such strong attitude variations are coupled with very high deviations (reported in Fig. 9 as well) of the flown track with respect to the planned linear one. In this regard, we note once again that the motion errors reported in Fig. 9 were not intentionally induced and that the flight acquisition was planned to be without squint and as linear as possible. The acquired data have been focused through the two approaches described in Sections III and IV, according to the processing parameters collected in Table IV. In Fig. 10, left panel (A), we show the SAR image focused on the radar grid through the approach of Section IV. In particular, an azimuth-invariant processing squint angle (calculated with respect to a nominal straight track) equal to $-3.4°$ at midrange has been used (this value is overplotted with the red line in the

TABLE IV
ACQUISITION AND PROCESSING PARAMETERS OF EXPERIMENT 1 (INSAES4 DATASET)

Mean platform's velocity	120 m/s
Mean platform's altitude	5 km

Azimuth resolution	1 m
Range resolution	3 m
Output grid sampling (radar grid)	0.6 m (az.) × 3 m (rg.)
Output grid sampling (geographic grid)	1 m × 1 m

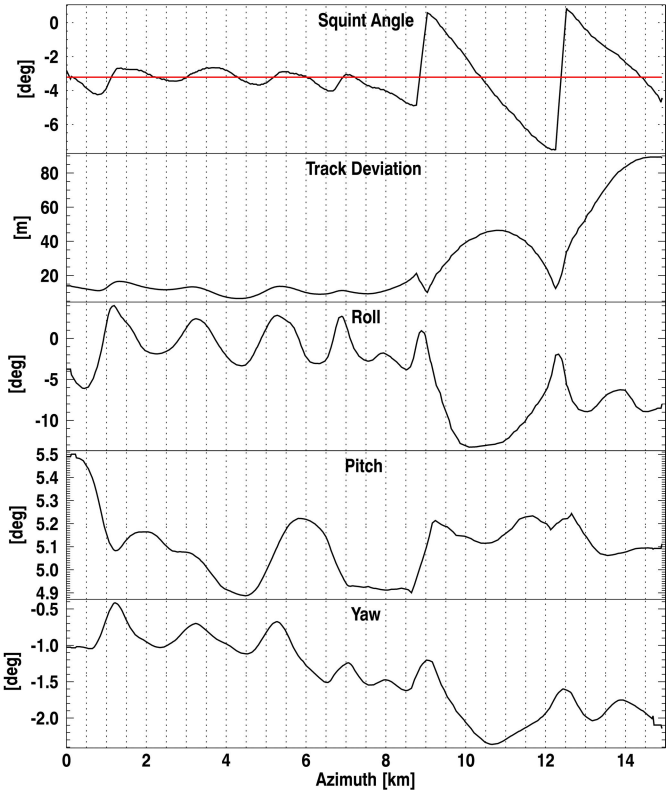

Fig. 9. InSAeS4 dataset: flight parameters relevant to the radar acquisition. From the top: squint angle at mid-range; track deviation (i.e., the distance between the actual flown track and the ideal straight track); roll; pitch; yaw. In the top panel, the red line represents the azimuth-invariant processing squint angle (calculated at the midrange) used to focus the data through the approach of Section IV.

top panel of Fig. 9). Note that this azimuth-invariant squint angle has been used also to generate the output radar grid [28].

In the right panel (C) of Fig. 10, instead, we show the SAR image focused through the approach of Section III, with a target-dependent processing squint angle equal to the acquisition one, thus accounting for the variable antenna pointing direction during the acquisition. As can be seen, the left SAR image presents some evident artifacts. First, an azimuth undulation of the amplitude. Second, a ghost at the top of the image highlighted with a red ellipse. To explain the origin of such artifacts, for each target, we first evaluated the LOS direction at the center of the corresponding synthetic aperture selected to focus the target according to the azimuth-invariant processing squint angle. Then, we calculated the angular separation between this direction and the beam center of

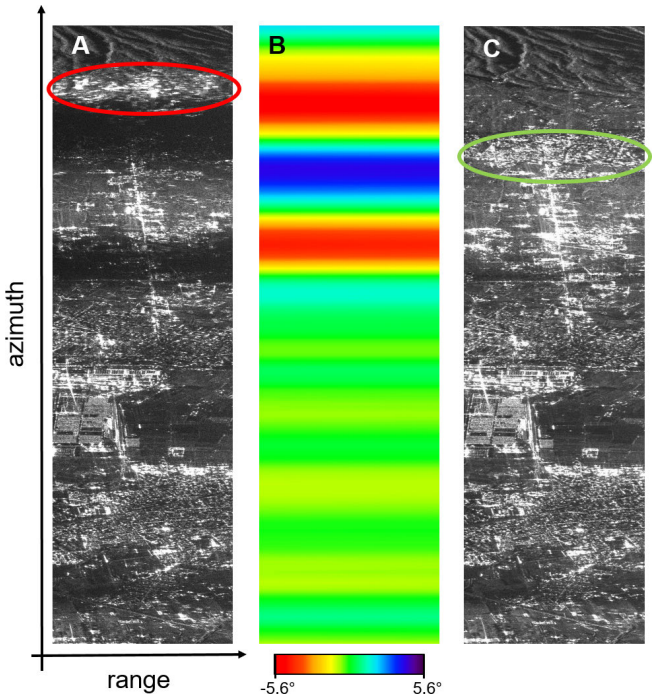

Fig. 10. InSAeS4 dataset: focusing results. (A) SAR image focused in radar grid with an azimuth-invariant processing squint angle. (B) Relevant to the focusing strategy adopted to obtain the image of (A): mismatch between the acquisition squint angle and the adopted azimuth-invariant processing squint angle. (C) SAR image focused in radar grid with a target-dependent processing squint angle. The main processing parameters are collected in Table IV.

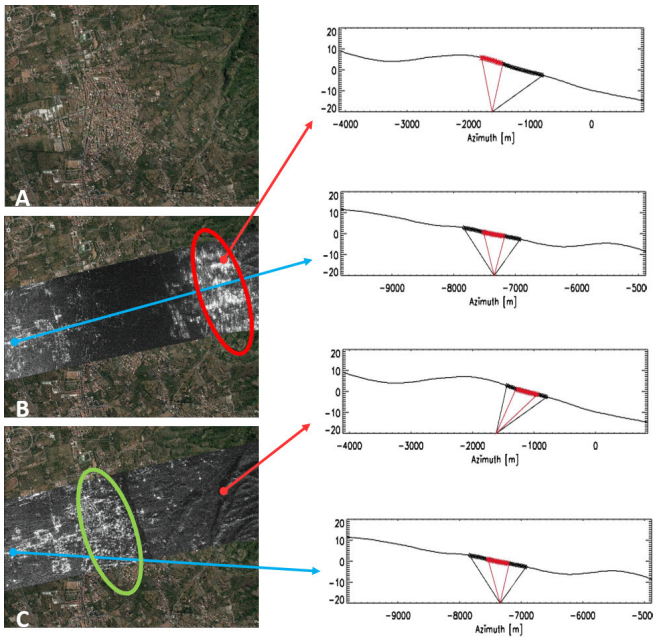

Fig. 11. Relevant to the top area of the InSAeS4 dataset of Fig. 10. (A) Optical image of the monitored area. (B) SAR image focused on a geographic grid with an azimuth-invariant processing squint angle. (C) SAR image focused on a geographic grid with a target-dependent processing squint angle. The main processing parameters are collected in Table IV. In both SAR images, two pixels are selected. For each pixel, we show, for each azimuth sensor coordinate, the angular separation (in degrees) between the antenna pointing direction and the direction from which the radar antenna illuminates the target. Moreover, in the plots, it is highlighted the track portion from which the radar antenna illuminates the considered target within the major beam (black), and the track portion selected by the algorithm to focus the target (red).

the antenna azimuth pattern. Thus, for each target, we have calculated the quantity in (5) sampled for $n = k_{\mathrm{ai}}$, that is,

$$\varphi_{k_{\mathrm{ai}}}(\vec{T}) = \frac{\pi}{2} - \operatorname{acos}\left[\hat{S}_{k_{\mathrm{ai}}} \cdot \hat{R}_{K_{\mathrm{ai}}}(\vec{T})\right] \tag{13}$$

where k_{ai} is the index in (2) calculated according to the optimization problem in (11) based on the azimuth-invariant processing squint angle approach. Note that the angle in (13) represents the separation between the azimuth beam center and the azimuth beam angle under which the target $\vec{T}$ is illuminated by the antenna at the center of the synthetic aperture selected to focus the target with the azimuth-invariant processing squint angle. In other words, the parameter in (13) allows measuring, for each target, the mismatch between the acquisition squint angle and the azimuth-invariant processing squint angle adopted to focus the target itself. The map of the angular separation in (13) relevant to all the targets of the scene considered in the SAR images of Fig. 10 is reported in the central panel (B) of the same figure. As expected, such a map presents azimuth undulations that follow those observed in the SAR image reported in the left panel. Note, in particular, that in correspondence to the ghost observed in the top area of the SAR image in the left panel of Fig. 10, the angular separation of the map reported in the central panel is on the order of the $\pm 2.8°$ limits that mark the beamwidth of the two-way antenna azimuth pattern. This means that when using an azimuth-invariant processing squint angle (as in the left SAR image), to focus a generic target belonging to this area, a nonnegligible portion of the selected synthetic aperture consists of track points from which the radar antenna illuminates the target outside the azimuth major beam. This clearly impairs the quality of the focused image.

To further analyze this issue, let us consider Fig. 11, where the top region of the area shown in Fig. 10 is reported on a geographic grid. In particular, the top panel (A) of Fig. 11 shows the optical image of the investigated area, whereas the other two panels report the georeferenced counterparts of the SAR images shown in Fig. 10. Specifically, the central (B) and bottom (C) panels show the SAR image focused with an azimuth-invariant and a target-dependent processing squint angle equal to the acquisition one, respectively. Comparison between the three panels of Fig. 11 clearly shows that the bright area highlighted with the red ellipse in the SAR image focused with an azimuth-invariant processing squint angle is a ghost image. Moreover, Figs. 10 and 11 show that the artifacts visible in the SAR image focused with an azimuth-invariant processing squint angle disappear in the SAR image obtained with a target-dependent processing squint angle equal to the acquisition one. Note also that the urban area highlighted with green ellipses (in Figs. 10 and 11) in the SAR image obtained with a target-dependent processing squint angle is lost in the SAR image obtained with an azimuth-variant processing squint angle equal to the acquisition one. To provide more insights into these aspects, in both SAR images of Fig. 11, two targets are selected: one highlighted in red and the other one in cyan.

TABLE V
ACQUISITION AND PROCESSING PARAMETERS OF EXPERIMENT 2 (AXIS DATASET)

Mean platform's velocity	45 m/s
Mean platform's altitude	2.5 km

Azimuth resolution	0.65 m
Range resolution	0.75 m
Output grid sampling (radar grid)	0.6 m (az.) × 0.75 m (rg.)

For each target, for both images, we plot, for each azimuth sensor coordinate, the angular separation between the antenna pointing direction and the direction from which the radar antenna illuminates the target. Moreover, in the plots, it is highlighted (black) the track portion from which the radar antenna illuminates the target within the major beam, that is, within the $\pm 2.8^\circ$ angular region centered around the azimuth beam center. The track portion selected by the algorithm to focus the target is also highlighted (red) in the plots. Let us start from the image focused with an azimuth-invariant squint angle (panel B). For the cyan pixel, the track portion selected to focus the pixel falls within the track portion from which the radar antenna illuminates the considered target within the major beam (see the plot indicated by the cyan arrow). This means that for this target, the azimuth-invariant processing squint angle that is used well approximates the acquisition squint angle. Indeed, the considered pixel belongs to an area where no significant focusing aberration occurs (see the SAR image of panel B). Instead, for the red pixel, which belongs to the area where the ghost appears, the track portion selected to focus the pixel falls outside the track portion from which the radar antenna illuminates the considered target within the major beam (see the plot indicated by the red arrow). This means that, for this target, the used azimuth-invariant processing squint angle is not appropriate for the actual acquisition squint angle. Let us now turn to the image focused with a target-dependent squint angle equal to the acquisition one (Fig. 11, panel C). As required, for both the considered targets, the same behavior is observed in the corresponding plots reported on the right, that is, the track portion selected to focus the target always falls within the portion from which the radar antenna illuminates the target within the major beam. Indeed, no focusing aberration occurs in the SAR image, which turns out to be well focused, despite the presence of the platform's very severe attitude variations characterizing the radar acquisition.

The second experiment is relevant to an AXIS dataset acquired in 2018 in the city of Salerno, Southern Italy. Also in this case, the acquisition, 20 km long in the azimuth direction, is characterized by very strong attitude variations (see Fig. 12). As can be seen, during the acquisition the roll varies from -6° to 1°, the pitch from -4° to -1.5°, and the yaw from 1° to 3°. This has led to the azimuth variations of the squint angle reported in the top panel of the figure, which is relevant, as usual, to the midrange. As can be seen, the squint angle varies approximately from -4° to 1° during the acquisition. Also in this case, such variations are particularly severe if compared with the azimuth beamwidth of the two-way antenna

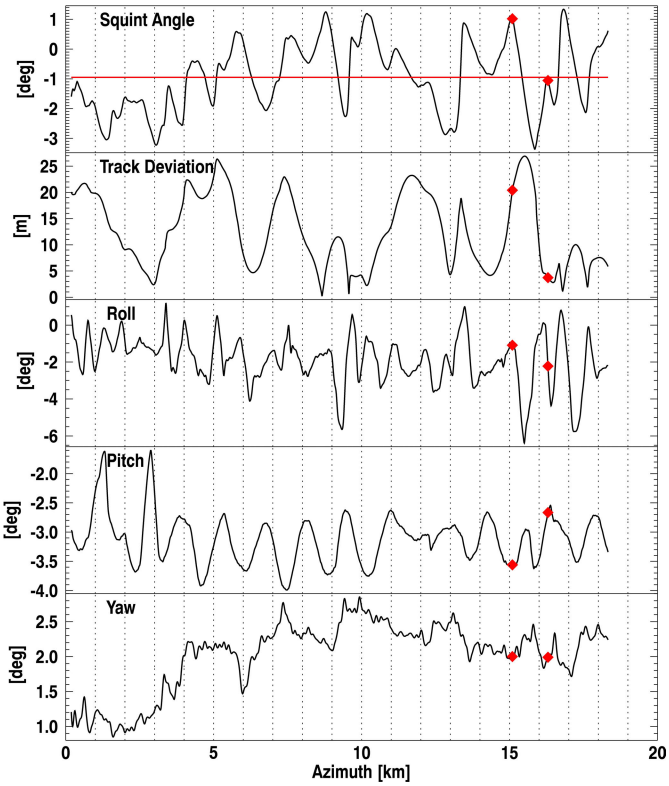

Fig. 12. AXIS dataset: flight parameters relevant to the radar acquisition. From the top: squint angle at midrange; track deviation (i.e., the distance between the actual flown track and the ideal straight track); roll; pitch; yaw. In the top panel, the red line represents the azimuth-invariant processing squint angle (calculated at the midrange) used to focus the data through the approach of Section IV. In all the panels, the two red diamonds mark the azimuth portion of the area considered in Fig. 13.

pattern, which is 5.2°. Furthermore, such attitude variations are coupled with high track deviations (see Fig. 12). We note once again that the motion errors reported in Fig. 12 were not intentionally induced. As in the InSAeS4 case, also the AXIS dataset has been focused through the two approaches described in Sections III and IV. Processing parameters are collected in Table V. In Fig. 13, in the left (A) and right (C) panels, we report the SAR image focused on the radar grid through the approaches of Sections III and IV, respectively. In particular, to focus the image of the left panel (A), an azimuth-invariant processing squint angle (calculated with respect to a nominal straight track) equal to -0.9° at midrange has been used (this value is overplotted with the red line in the top panel of Fig. 12). As usual, such azimuth-invariant squint angle has been used also to generate the output radar grid [28]. We emphasize that, although the entire dataset has been focused, we investigate in the figure just a part of the overall image corresponding to the track portion between the two red diamonds in Fig. 12. As for Fig. 10, in the central panel (B) of Fig. 13, we report the map of the angular separation in (13) relevant to all the targets of the SAR images of the same figure. We find that the SAR image focused with an azimuth-invariant processing squint angle (panel A and the corresponding zoom on the left) presents a ghost in correspondence to the port; on the other side, such an artifact disappears in the SAR image obtained with a target-dependent processing squint angle equal to the acquisition one (panel C and the corresponding zoom

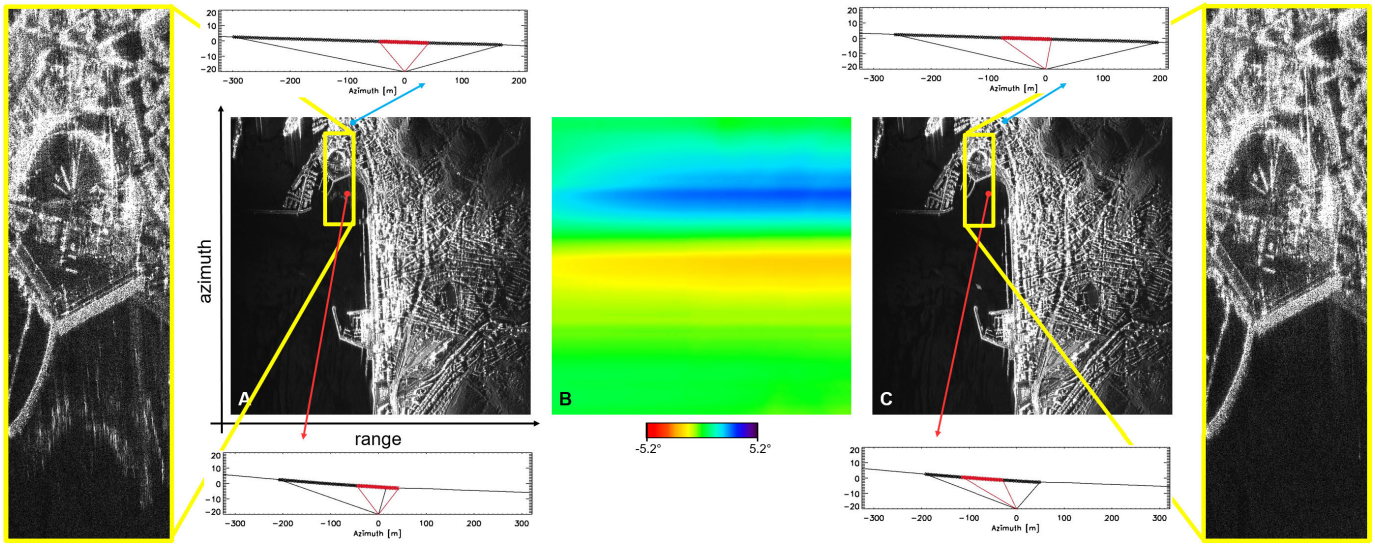

Fig. 13. AXIS dataset: focusing results. (A) SAR image focused in radar grid with an azimuth-invariant processing squint angle, with highlighted on the left a zoom of the port area. (B) Relevant to the focusing strategy adopted to obtain the image of the panel (A): mismatch between the acquisition squint angle and the adopted azimuth-invariant processing squint angle. (C) SAR image focused on the radar grid with a target-dependent processing squint angle, with highlighted on the right a zoom of the port area. Main processing parameters are collected in Table V. Two pixels are selected in both SAR images. For each pixel, we plot for each azimuth sensor coordinate, the angular separation (in degrees) between the antenna pointing direction and the direction from which the radar antenna illuminates the target. Moreover, the plots show the track portion from which the radar antenna illuminates the target within the major beam (black), and the track portion selected by the algorithm to focus the target (red).

on the right). Also, in this case, the origin of the artifact affecting the left SAR image can be explained through the map reported in the central panel. Indeed, in correspondence to the ghost observed in the SAR image, the angular separation in (13) is on the same order as the $\pm 2.6°$ limits that mark the beamwidth of the two-way antenna azimuth pattern. Once again, this means that when exploiting an azimuth-invariant processing squint angle, to focus a generic target belonging to this area, a nonnegligible portion of the selected synthetic aperture consists of track points from which the radar antenna illuminates the target outside the azimuth major beam. To better clarify this issue, as in Fig. 11, also in this case, two pixels are selected in both SAR images, and for each pixel, we show a plot for each azimuth sensor coordinate (calculated with respect to the generated output radar grid), the angular separation between the antenna pointing direction and the direction from which the radar antenna illuminates the target. As in Fig. 11, in all the plots, it is also highlighted the track portion from which the radar antenna illuminates the selected target within the major beam (black), and the track portion selected by the algorithm to focus the target (red). As seen in panel (A), for the cyan pixel, which belongs to an area where no significant focusing aberration occurs, the applied azimuth-invariant processing squint angle well approximates the acquisition squint angle (see the corresponding plot indicated by the cyan arrow). Instead, for the red pixel belonging to the area where the ghost appears, the applied azimuth-invariant processing squint angle is not appropriate for the actual acquisition squint angle (see the corresponding plot indicated by the red arrow). Turning instead to panel (C), as required, the selected synthetic aperture always falls within the portion from which the radar antenna illuminates the target within the major beam. Once again, no focusing aberrations occur in the SAR image, despite the presence of the platform's attitude variations reported in Fig. 12.

VI. Interferometric SAR Focusing and Target-Dependent Processing Squint Angle

In Section V, we have shown that, to obtain accurate focusing in the presence of strong platform attitude variations, the approach based on the use of an azimuth-invariant processing squint angle may become unsuitable, whereas the use of a target-dependent processing squint angle, equal to the acquisition one, is appropriate. In this section, we show how to revise the latter focusing strategy for interferometric purposes. To this aim, in the following, we focus on a cross-eyed single-pass interferometric configuration. In particular, we consider the second dataset analyzed in Section V, that is, the AXIS one. Indeed, in this case, an angular separation of 1.2° occurred between the boresight planes of the two Rx antennas forming the interferometric layout. It is noted that such a cross-eyed configuration unintentionally occurred when mounting the radar system along with the corresponding antennas on the Cessna 172 airplane before the acquisition campaign [16]. It is also stressed that such installation problems may often occur in an increasingly widespread class of aerial SAR missions that involve compact and lightweight systems, to be mounted just before the beginning (and unmounted just after the end) of SAR acquisition campaigns operated through small and flexible aerial platforms [7]. According to the analysis presented Section V, the two interferometric channels have been focused with a target-dependent processing squint angle, again with the processing parameters collected in Table V. However, due to the cross-eyed interferometric layout discussed above, for each target, the corresponding acquisition squint angle (and thus the processing one used

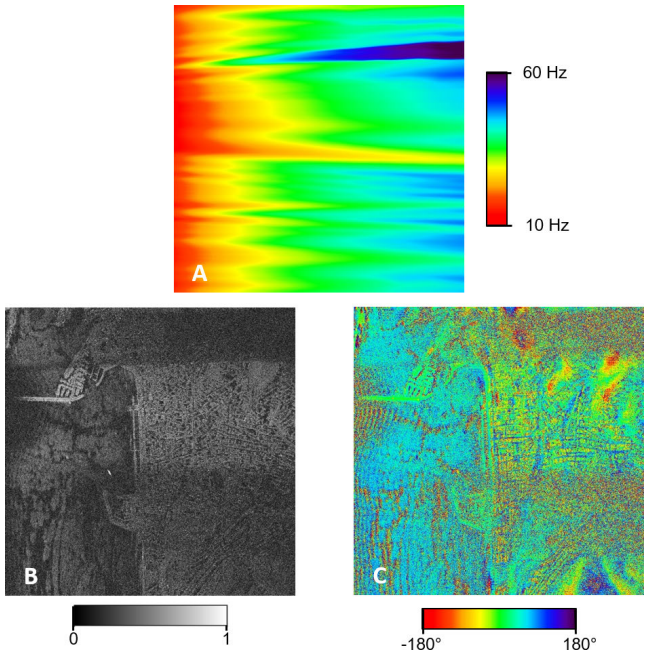

Fig. 14. AXIS interferometric dataset: focusing the main and the secondary image with two different target-dependent squint angles, each tailored to the corresponding acquisition squint angle of the channel. (A) Target-dependent separation between the acquisition Doppler centroids of the two channels. (B) Computed interferometric coherence. (C) Computed interferogram. The main processing parameters are collected in Table V.

during the focusing) turned out to be different for the two channels. This has led to a target-dependent relative shift of the processing Doppler centroids used to focus the two interferometric images. It is noted that this scenario, which is not peculiar to single-pass interferometric acquisitions carried out with well-oriented antennas, is instead very common, and typically much more critical, in repeat-pass interferometric acquisitions, where the platform attitude variations affecting the two flights are generally very different from each other. In our cross-eyed single-pass configuration, the amount of the Doppler centroid shift between the two channels and relevant to each target is shown in Fig. 14(A). In particular, for each target, the reported values have been obtained from the corresponding difference between the acquisition squint angles calculated for the two channels of the bistatic system at hand. As it can be seen, this shift ranges approximately from 10 to 60 Hz, which are quite severe values if compared with the 70 Hz of the processing Doppler bandwidth needed to obtain the 0.65-m azimuth resolution (see Table V). As a consequence, the interferometric coherence, which is shown in Fig. 14(B) as well, is impaired, especially in those areas where the separation between the Doppler centroids is in the same order as the adopted processing Doppler bandwidth. In these areas, the quality of the corresponding interferogram, reported in Fig. 14(C), is of course impaired. Summing up, when the acquisition squint angles are different in the two interferometric channels, the strategy adopted to separately obtain accurate focusing of the two different channels by separately following the azimuth variations of the squint angles relevant to the two different channels is not appropriate for interferometric purposes.

To circumvent this effect, one can think to pursue the spectral overlapping between the processing Doppler bandwidths of the two interferometric channels by enlarging, as much as possible, their extensions. In other words, one can think to separately focus the two interferometric images, still with a target-dependent processing angle equal to the acquisition one, by pursuing the finest possible azimuth resolution imposed by the two-way antenna beamwidth (which is in airborne SAR systems, often wider than that strictly needed to obtain the azimuth resolution required by the application of interest). Then the common part (if existing) of the Doppler spectrum is selected in each image within the interferometric processing. This strategy, however, typically involves a strong computational effort during the focusing step and requires, for each interferometric image, the implementation of an azimuth variant Doppler filtering, whose application is not straightforward.

Another strategy, more efficient from the computational point of view, is instead to retain the required azimuth resolution (without pursuing the finest one) and to select the common part of the processing Doppler bandwidths of the two interferometric channels during (rather than after) the focusing step. To do this, the two images of the interferometric pair must be focused with the required resolution, still with a target-dependent processing angle. However, for each target, this processing squint angle is the same for the main and the secondary image. In particular, for the considered cross-eyed single-pass interferometric configuration (where the velocities of the main and secondary antennas can be safely assumed equal to each other), this common processing squint angle is given by

$$\Phi_p(\vec{T}) = \frac{\Phi_m(\vec{T}) + \Phi_s(\vec{T})}{2} \tag{14}$$

where $\Phi_m(\cdot)$ and $\Phi_s(\cdot)$ are the acquisition squint angles of the main and secondary channels, respectively. The latter strategy can be straightforwardly implemented following the block diagram of Fig. 15, which basically consists of two steps. The first step, the target-dependent procedure described in Section III is separately applied for the main and the secondary images according to the block diagram of Fig. 5. For each target $\vec{T}$, this leads to the computation of the indexes $k_m(\vec{T})$ and $k_s(\vec{T})$ defining the two acquisition squint angles $\Phi_m(\cdot)$ and $\Phi_s(\cdot)$, respectively. The second step sets the processing squint angle in (14) by computing, for both the main and the secondary channels, the same common index k in (2) as follows (see Appendix D):

$$k_{\text{inf}}(\vec{T}) = \frac{k_m(\vec{T}) + k_s(\vec{T})}{2} \tag{15}$$

where the subscript inf stands for interferometric.

The considered interferometric case is depicted in Fig. 16, where $\overrightarrow{\text{MA}}$ and $\overrightarrow{\text{SA}}$ are the positions of the main and secondary APCs, respectively. In the figure, the two acquisition squint angles of the two interferometric channels are different from

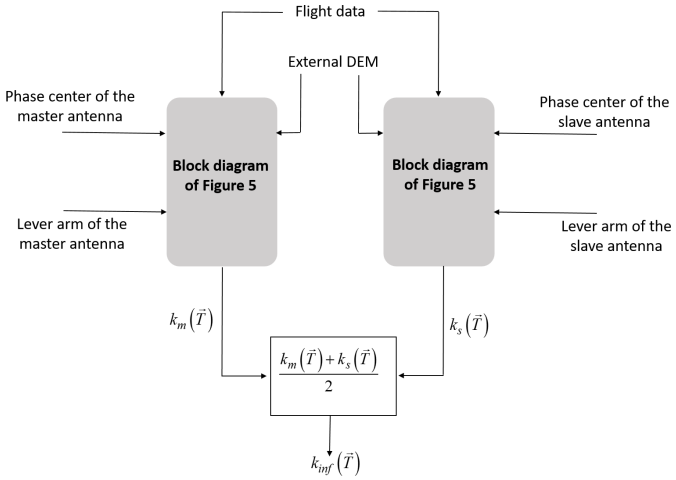

Fig. 15. Block diagram of the interferometric SAR focusing approach in the time domain with a target-dependent processing squint angle: calculation of the index k_{inf} in (15) for a cross-eyed single-pass interferometric configuration.

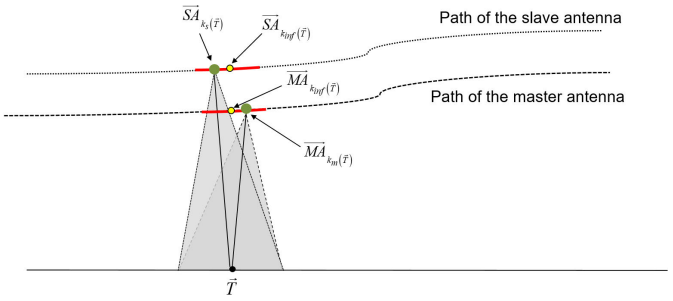

Fig. 16. Interferometric SAR focusing with target-dependent processing squint angle: cross-eyed single-pass interferometric configuration. The two positions from which the main and the secondary radar antennas illuminate at their azimuth beam center the target $\vec{T}$ are highlighted with green points. For each interferometric channel, the synthetic aperture used to focus the target is highlighted in red and its center is represented by a yellow point. Note that in this case, the corresponding yellow and green points are not coincident.

each other: to match at best both acquisition geometries, the same processing squint angle, lying halfway between these two acquisition angles, is adopted for both channels. Of course, if the separation between the acquisition Doppler centroids of the two channels is less than the Doppler bandwidth associated with the overall two-way azimuth beamwidth then, for each interferometric channel, the selected synthetic aperture still falls within the track portion from which the radar antenna illuminates the considered target within the major beam.

The procedure described by the block diagram of Fig. 15 has been applied to the dataset of Fig. 13, by considering the processing parameters collected in Table V. The achieved results are reported in Fig. 17, where the interferometric coherence (panel C) is clearly greater than the corresponding one shown in Fig. 14, as shown by the two histogram envelopes in Fig. 18. Accordingly, the quality of the obtained interferogram (panel D) is significantly improved with respect to that in Fig. 14. Moreover, in Fig. 17, for both the main (panel A) and secondary (panel B) image, we have also reported the maps of the angular separation in (13) obtained with the applied focusing approach. As expected, the two maps are not identically null, as would happen if we separately focused the two images, each with its target-dependent processing squint angle equal to the corresponding acquisition one. This confirms that we moved toward a focusing paradigm, say interferometric focusing, which is appropriate to obtain high interferometric coherence, and suboptimal to separately focus the two interferometric channels. It is finally emphasized that the angular separation reported in both maps is significantly smaller than that of the corresponding map reported in Fig. 13(B) which has been obtained by focusing the main image with an azimuth-invariant processing squint angle. This confirms that, from the image formation point of

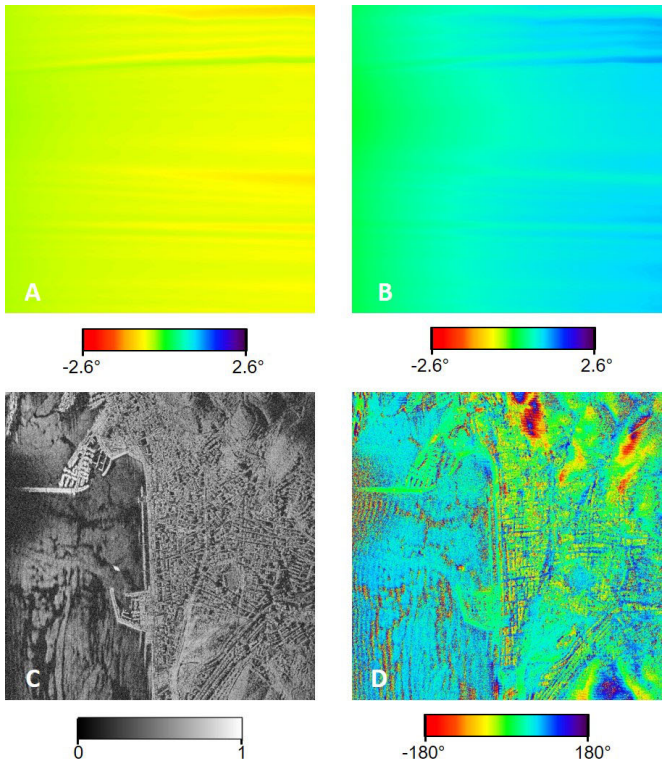

Fig. 17. AXIS interferometric dataset: focusing the main and the secondary image with the same target-dependent squint angle lying halfway between the two different acquisition squint angles of the two channels. (A) Mismatch between the acquisition squint angle of the main channel and the adopted target-dependent processing squint angle. (B) As in (A), but for the secondary channel. (C) Computed interferometric coherence. (D) Computed interferogram. The main processing parameters are collected in Table V.

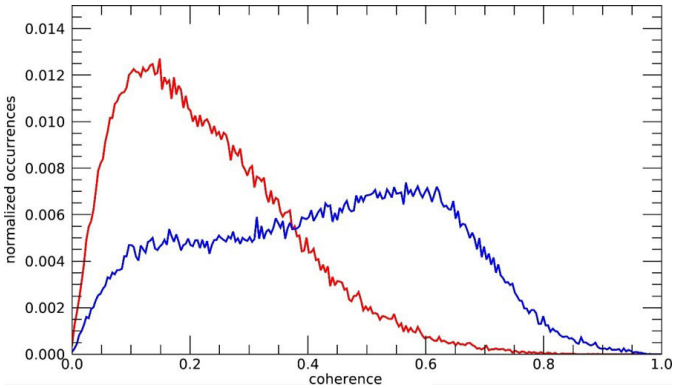

Fig. 18. Histogram envelopes relevant to the coherence maps of Figs. 14 (red line) and 17 (blue line).

view, the adopted interferometric focusing strategy is, in any case, more appropriate than the focusing carried out with an azimuth-invariant squint angle.

VII. Conclusion

In this work, the problems related to the focusing of airborne SAR data in the presence of strong azimuth variations of the squint angle have been addressed. To this aim, a time-domain SAR focusing algorithm, based on using a target-dependent processing squint angle, has been developed and applied to real data acquired by two different airborne SAR systems operating at X-band. For comparison purposes, also a time-domain SAR processor based on using an azimuth-invariant processing squint angle has been developed and applied.

The presented experiments have shown that the adoption of an azimuth-invariant processing squint angle, typically pursued by computationally efficient focusing strategies, is inappropriate in the case of airborne acquisitions affected by motion errors leading to azimuth variations of the squint angle on the same order of magnitude of the two-way azimuth beamwidth of the radar antenna. It is also stressed that such motion errors are unwanted aberrations induced by unavoidable atmospheric turbulences affecting typical airborne SAR acquisitions, thus inducing a deviation with respect to the original mission plans generally requesting radar acquisitions carried out without a squint angle and with linear flight tracks. In particular, such strong motion errors may affect flight acquisitions independently of the dimension of the airplane, its velocity, or the flight altitude. For instance, the InSAeS4 data acquisition considered in this work, although planned without squint over a linear track (15 km long), is in reality characterized by variations of the squint angle on the order of 10°, which are very severe if compared with the two-way azimuth beamwidth of the radar antenna (5.6°). In this case, the radar system embedding an accurate navigation unit was mounted onboard a rather big airplane, namely, a Learjet, flying at a 5 km altitude at a mean velocity of 120 m/s. Similarly, the AXIS data acquisition considered in this work, again planned without squint over a linear track (20 km long), is in reality characterized by variations of the squint angle on the order of 6°, which are again very strong considering the two-way azimuth beamwidth of the radar antenna (5.2°). In this case, the radar system, also embedding an accurate navigation unit, was instead mounted onboard a small airplane, namely a Cessna 172, flying at 2.5 km altitude at a mean velocity of 45 m/s. For both datasets, it has been shown that the focusing approach based on the use of an azimuth-invariant processing squint angle is unsuitable, since the obtained SAR images are corrupted by different artifacts, such as undesired amplitude azimuth modulations and/or ghosts. Moreover, it has been shown that all these problems are circumvented by exploiting the implemented focusing approach based on the use of a target-dependent processing squint angle capable of accounting for the variations of the pointing direction of the radar antenna during the acquisition.

We further remark that the presented experiments, carried out through a cross-eyed single-pass interferometric configuration, have shown that such a focusing strategy should be properly revised in the case of interferometric processing. Indeed, when the acquisition squint angles of the two interferometric channels are different, as happens in single-pass cross-eyed configurations or in the repeat-pass case, we have to move toward a different focusing paradigm, say interferometric focusing. In this case, the focusing is still based on the use of a target-dependent processing squint angle, which is the same for the two images and lies halfway between the two different acquisition squint angles of the two interferometric channels. It has been shown that the interferometric focusing is appropriate to obtain high interferometric coherence, and suboptimal to separately focus the interferometric channels. Moreover, from the image formation point of view, the interferometric focusing strategy is in any case more appropriate than the focusing approach based on the use of an azimuth-invariant squint angle. The exploitation of the interferometric focusing strategy for the generation of time series based on the use of large datasets acquired through several repeat-pass acquisitions, where the platform track deviations and attitude variations affecting the different flights may be generally different from each other, is a matter of current study and future work.

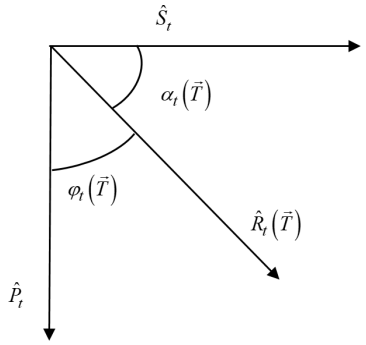

Fig. 19. Relevant to the optimization problem in (6).

Appendix A

In this appendix, we provide more insights on (5) and (6). To this aim, let us first assume the slow time to be continuous and refer to Fig. 19, where the unit vectors $\hat{S}_t$ in (3) and $\hat{R}_t(\vec{T})$, defined through (2), are represented. In this case, the subscript n adopted in (2) and (3) has been replaced by t, which represents the continuous slow time. The unit vector $\hat{P}_t$ orthogonal to $\hat{S}_t$ defines the boresight direction which we assume, without any loss of generality, to be coincident with the antenna azimuth beam center. The angle between $\hat{R}_t(\vec{T})$ and $\hat{S}_t$, $\alpha_t(\vec{T})$, is given by

$$\alpha_t(\vec{T}) = \operatorname{acos}\left[\hat{S}_t \cdot \hat{R}_t(\vec{T})\right]. \tag{16}$$

Note that the angle $\varphi_t(\vec{T})$ defined in (5) (with the usual substitution $t \to n$) is given by

$$\varphi_t(\vec{T}) = \frac{\pi}{2} - \alpha_t(\vec{T}). \tag{17}$$

When the radar antenna illuminates the target at the azimuth beam center, the vectors $\hat{R}_t(\vec{T})$ and $\hat{P}_t(\vec{T})$ become coincident, that is, $\hat{R}_t(\vec{T})$ and $\hat{S}_t$ become orthogonal. In this case,

we obtain

$$\alpha_t(\vec{T}) = \frac{\pi}{2} \tag{18}$$

and

$$\varphi_t(\vec{T}) = 0 \tag{19}$$

see (16) and (17). So, to find the time instant at which the target $\vec{T}$ is illuminated by the antenna at its beam center, we have to enforce the condition in (19) or, equivalently, the one in (18). When considering the discrete slow time, enforcement of condition (19) must be replaced by the numerical minimization in (6).

Appendix B

This appendix addresses the calculation of the antenna-to-target distance $R_n(\vec{T})$ in (2), and the unit vector $\hat{S}_n$ in (3). Calculation of the antenna-to-target distance $R_n(\vec{T})$ requires knowledge of the positions $\vec{T}$ and $\vec{A}_n$, see (1), in a common reference system.

The vector $\vec{T}$ is obtained from an available external DEM of the illuminated area. This vector is commonly provided with respect to the World Geodetic System (WGS) reference system.

The vector $\vec{A}_n$ is obtained starting from the flight data recorded by the navigation system, which typically embeds the IMU and the GNSS. In particular, the flight data provide the attitude information (namely, the roll, pitch, and yaw angles) of the platform as well as the position of the IMU phase center with respect to the WGS reference system. To calculate $\vec{A}_n$ in (1), starting from the flight data, three procedural steps are necessary. The first one is the calculation of the position of the radar APC with respect to a local reference system defined over the antenna itself. This operation is typically carried out in the laboratory [37], although other methods are possible as well [38]. The second step is the measurement of the so-called antenna lever arm, that is, the position of the APC with respect to a local reference system, centered in the IMU phase center, and defined within the aerial vehicle by the IMU itself. This operation is typically carried out through the theodolite technique when the radar antenna and the IMU are mounted onboard and the aerial vehicle is at rest [8], [16]. The third step performs the coordinate change of the APC position from the IMU reference system to the WGS one, through the use of the lever arm measurements along with the flight (position and attitude) data, see [29] for further details.

The calculation of the unit vector $\hat{S}_n$ in (3) is now in order. Following the definition of Section III, such a vector is oriented parallel to the azimuth antenna side (see Fig. 1). By referring to Fig. 20, let us consider the vector $\vec{S}_n$ associated with the unit vector $\hat{S}_n$

$$\vec{S}_n = \vec{C}_n^{\,\mathrm{ur}} - \vec{C}_n^{\,\mathrm{ul}} \tag{20}$$

where $\vec{C}_n^{\,\mathrm{ur}}$ and $\vec{C}_n^{\,\mathrm{ul}}$ are the positions of the two reference points of the antenna, namely, the two corners highlighted in Fig. 20. We stress that although Fig. 20 refers to planar antennas (which are very common in airborne SAR systems) where the adopted reference points can be easily found, similar reference points can be found in every antenna type, possibly using cradles similar to those commonly used for antenna measurement purposes. Equation (20) reduces our problem to the measurement, with respect to the WGS reference system, of the positions $\vec{C}_n^{\,\mathrm{ur}}$ and $\vec{C}_n^{\,\mathrm{ul}}$. This procedure is exactly the same as the one described above for the measurement of the vector $\vec{A}_n$, provided that the phase center of the antenna is substituted by the corners of the antenna itself. Once the vector $\vec{S}_n$ in (20) is measured, the calculation of the corresponding unit vector $\hat{S}_n$ is straightforward.

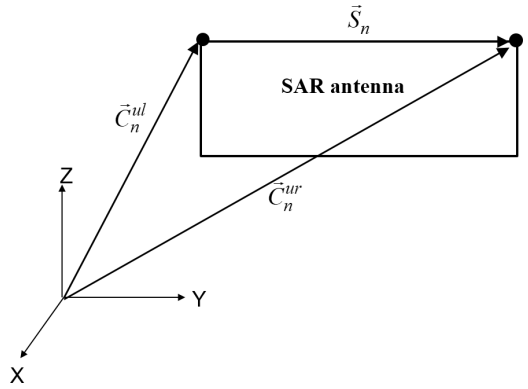

Fig. 20. Relevant to the calculation of the unit vector $\hat{S}_n$ in (3).

Appendix C

In this appendix, we show that under the following conditions:

1) constant antenna pointing direction during the acquisition;
2) linear flight path;
3) flat topography;

the squint angle becomes azimuth-independent.

From condition 1), we obtain that the orientation of the vector $\hat{S}_n$ and the plane $\mathscr{P}_n$ in Figs. 2 and 3 become independent of the slow time. Therefore, we can substitute the vector $\hat{S}_n$ with the n-independent vector $\hat{S}$, and the planes $\mathscr{P}_n$ with $\mathscr{P}$, which belongs to a bundle of parallel planes.

From condition 2), we obtain that the orientation of the unit vector $\hat{v}_n$ becomes independent of the slow time, and thus n-independent.

Accordingly, when the conditions 1) and 2) are satisfied, the expressions in (3) and (4) can be rewritten as follows:

$$\hat{S} \cdot \hat{R}_k(\vec{T}) = 0 \tag{21}$$

and

$$\Phi(\vec{T}) = \frac{\pi}{2} - \mathrm{acos}\left[\hat{v} \cdot \hat{R}_k(\vec{T})\right]. \tag{22}$$

Note that in the scalar product in (21) the first term is constant; therefore, to satisfy condition (21), the unit vector $\hat{R}_k(\vec{T})$ should belong to the plane $\mathscr{P}$, whose orientation is independent of the specific index k. Therefore, in the scalar product in (22), the second term lies on a plane whose orientation is independent of the specific index k; moreover, the first term is constant. For any target $\vec{T}$ and for any index k, the scalar product in (22) depends only on the elevation angle relevant to the target $\vec{T}$. Note also that such elevation angle is

related to the topographic elevation of the considered target, thus on both its azimuth and range coordinates. However, when condition 3) is enforced, the direction of the unit vector $\hat{R}_k(\vec{T})$ becomes independent of the azimuth coordinate of the target $\vec{T}$, and it depends only on its range coordinate. Accordingly, when conditions 1)–3) are simultaneously satisfied, the squint angle in (22) becomes azimuth-independent.

A final consideration is in order.

It is observed that the dependence of the squint angle from the topography of the observed area is strongly related to the altitude of the SAR sensor. In particular, such dependence is much lower in spaceborne systems, which operate at altitudes of hundreds of kilometers, than in aerial systems, which instead operate at significantly lower altitudes. In the former case, indeed, the variation of the elevation angle (and thus, of the squint angle) corresponding to a given topographic profile is much lower.

Appendix D

In this appendix, we show that in a cross-eyed single-pass interferometric configuration, to set the processing squint angle as in (14), the index k in (2) must be computed, for both the main and the secondary channels, as in (15). To this aim, let us refer to Fig. 21, where the acquisition geometry in a cross-eyed single-pass interferometric configuration is depicted. In this figure, $\overrightarrow{\mathrm{MA}}$ and $\overrightarrow{\mathrm{SA}}$ are the positions of the main and secondary APCs. Φ_m and Φ_s are the acquisition squint angles of the main and secondary channels, respectively, whereas Φ_p is the common processing squint angle evaluated according to (14). For the sake of simplicity, in Fig. 21, we omitted the dependence of these quantities on the target position $\vec{T}$. Moreover, in Fig. 21, we have highlighted in green the two positions from which the two radar antennas illuminate at their azimuth beam center the considered target. These two positions are defined by the indexes k_m and k_s, respectively, computed according to the block diagram of Fig. 15. The two points highlighted in yellow in Fig. 21 represent instead the centers of the processed synthetic apertures for the main and secondary images, respectively, corresponding to the common processing squint angle Φ_p in (14).

Note that the velocities $\vec{v}$ of the main and secondary antennas are equal, since the interferometric configuration is single-pass. It is also noted that, locally, the vector $\vec{v}$ defines the azimuth direction of the acquisition geometry. In this regard, the distance a in the figure represents the azimuth separation between the two green points.

The light-blue and light-green triangles in the figure are not coplanar; however, they share the direction of the two horizontal cathetuses.

The angles Φ_m and Φ_s are given by

$$\Phi_m = \operatorname{atan}\left(\frac{a+b}{r_0}\right) \approx \frac{a+b}{r_0} \tag{23}$$

and

$$\Phi_s = \operatorname{atan}\left(\frac{b}{r_0+\delta r}\right) \approx \frac{b}{r_0+\delta r} \approx \frac{b}{r_0}. \tag{24}$$

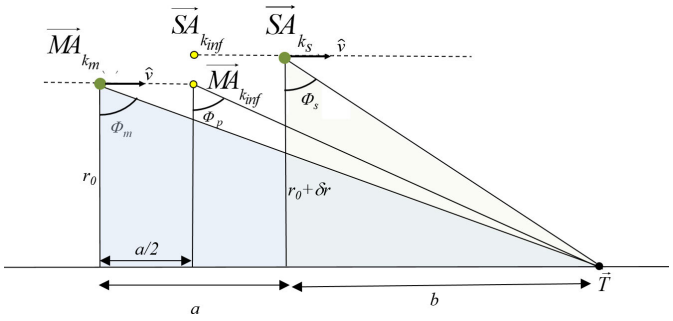

Fig. 21. Acquisition geometry in a cross-eyed single-pass interferometric configuration. Distances not to scale.

Use of (23) and (24) in (14) leads to

$$\Phi_p = \frac{\Phi_m + \Phi_s}{2} \approx \frac{\frac{a}{2}+b}{r_0} \tag{25}$$

which implies that, for the main image, the azimuth coordinate of the center of the processed synthetic aperture (yellow point $\overrightarrow{\mathrm{MA}}_{k_{\mathrm{inf}}}$ in the figure) lies halfway between the azimuth coordinates of the two green points $\overrightarrow{\mathrm{MA}}_{k_m}$ and $\overrightarrow{\mathrm{SA}}_{k_s}$. The index k_{inf} associated with the point $\overrightarrow{\mathrm{MA}}_{k_{\mathrm{inf}}}$ is thus given by (15). Note that (24) can be safely approximated as follows:

$$\Phi_p \approx \frac{\frac{a}{2}+b}{r_0+\delta r} \tag{26}$$

which allows us to repeat the analysis above also for the point $\overrightarrow{\mathrm{SA}}_{k_{\mathrm{inf}}}$ in Fig. 21, which is the center of the processed synthetic aperture for the secondary image. Therefore, the index k_{inf} associated with the point $\overrightarrow{\mathrm{SA}}_{k_{\mathrm{inf}}}$ is given by (15) as well.

Acknowledgment

The authors would like to thank Dr. Paul R. Lundgren of JPL, California Institute of Technology, for proofreading the paper and the anonymous reviewers and the editor for the valuable comments and suggestions. Finally, they thank S. Guarino, F. Parisi, and M.C. Rasulo for their support.

References

[1] G. Franceschetti and R. Lanari, *Synthetic Aperture Radar Processing*. New York, NY, USA: CRC Press, 1999.

[2] A. Moreira, P. Prats-Iraola, M. Younis, G. Krieger, I. Hajnsek, and K. P. Papathanassiou, "A tutorial on synthetic aperture radar," *IEEE Geosci. Remote Sens. Mag.*, vol. 1, no. 1, pp. 6–43, Mar. 2013.

[3] D. Tarchi et al., "Landslide monitoring by using ground-based SAR interferometry: An example of application to the Tessina landslide in Italy," *Eng. Geol.*, vol. 68, nos. 1–2, pp. 15–30, 2003.

[4] M. Virelli, A. Coletta, and M. L. Battagliere, "ASI COSMO-SkyMed: Mission overview and data exploitation," *IEEE Geosci. Remote Sens. Mag.*, vol. 2, no. 2, pp. 64–66, Jun. 2014.

[5] G. Krieger et al., "TanDEM-X: A satellite formation for high-resolution SAR interferometry," *IEEE Trans. Geosci. Remote Sens.*, vol. 45, no. 11, pp. 3317–3341, Nov. 2007.

[6] R. Torres et al., "GMES Sentinel-1 mission," *Remote Sens. Environ.*, vol. 120, pp. 9–24, May 2012.

[7] S. Perna, F. Soldovieri, and M. Amin, "Editorial for Special Issue 'Radar imaging in challenging scenarios from smart and flexible platforms,'" *Remote Sensing*, vol. 12, no. 8, p. 1272, 2020, doi: 10.3390/rs12081272.

[8] C. Wimmer, R. Siegmund, M. Schwabisch, and J. Moreira, "Generation of high precision DEMs of the Wadden Sea with airborne interferometric SAR," *IEEE Trans. Geosci. Remote Sens.*, vol. 38, no. 5, pp. 2234–2245, Sep. 2000.

[9] S. Hensley et al., "First P-band results using the GeoSAR mapping system," in *Proc. Int. Geosci. Remote Sens. Symp.*, Sydney, NSW, Australia, vol. 1, Jul. 2001, pp. 126–128.

[10] L. M. H. Ulander et al., "Development of the ultra-wideband LoRa SAR operating in the VHF/UHF-band," in *Proc. IEEE Int. Geosci. Remote Sens. Symp. (IGARSS)*, vol. 7, Jul. 2003, pp. 4268–4270.

[11] S. Perna and C. Wimmer, "X-band airborne differential interferometry: Results of the OrbiSAR campaign over the Perugia area," *IEEE Trans. Geosci. Remote Sens.*, vol. 46, no. 2, pp. 489–503, Feb. 2008.

[12] C. Magnard, M. Frioud, D. Small, T. Brehm, H. Essen, and E. Meier, "Processing of MEMPHIS Ka-band multibaseline interferometric SAR data: From raw data to digital surface models," *IEEE J. Sel. Topics Appl. Earth Observ. Remote Sens.*, vol. 7, no. 7, pp. 2927–2941, Jul. 2014.

[13] O. R. D. Plessis et al., "ONERA SAR facilities," *IEEE Aerosp. Electron. Syst. Mag.*, vol. 26, no. 11, pp. 24–30, Nov. 2011.

[14] S. Perna et al., "The InSAeS4 airborne X-band interferometric SAR system: A first assessment on its imaging and topographic mapping capabilities," *Remote Sens.*, vol. 8, no. 1, p. 40, Jan. 2016.

[15] M. Pinheiro, A. Reigber, R. Scheiber, P. Prats-Iraola, and A. Moreira, "Generation of highly accurate DEMs over flat areas by means of dual-frequency and dual-baseline airborne SAR interferometry," *IEEE Trans. Geosci. Remote Sens.*, vol. 56, no. 8, pp. 4361–4390, Aug. 2018.

[16] C. Esposito, A. Natale, G. Palmese, P. Berardino, R. Lanari, and S. Perna, "On the capabilities of the Italian airborne FMCW AXIS InSAR system," *Remote Sens.*, vol. 12, no. 3, p. 539, Feb. 2020.

[17] S. Perna et al., "The ASI integrated sounder-SAR system operating in the UHF–VHF bands: First results of the 2018 helicopter-borne Morocco desert campaign," *Remote Sens.*, vol. 11, no. 16, p. 1845, Aug. 2019.

[18] P. Rosen et al., "UAVSAR: New NASA airborne SAR system for research," *IEEE Aerosp. Electron. Syst. Mag.*, vol. 22, no. 98, pp. 21–28, Nov. 2007.

[19] A. Aguasca, R. Acevo-Herrera, A. Broquetas, J. Mallorqui, and X. Fabregas, "ARBRES: Light-weight CW/FM SAR sensors for small UAVs," *Sensors*, vol. 13, no. 3, pp. 3204–3216, Mar. 2013.

[20] D. Kim, S. Hensley, S. Yun, and M. Neumann, "Detection of durable and permanent changes in urban areas using multitemporal polarimetric UAVSAR data," *IEEE Geosci. Remote Sens. Lett.*, vol. 13, no. 2, pp. 267–271, Feb. 2016.

[21] D. Luebeck et al., "Drone-borne differential SAR interferometry," *Remote Sens.*, vol. 12, no. 5, p. 778, Feb. 2020.

[22] A. Moreira and Y. Huang, "Airborne SAR processing of highly squinted data using a chirp scaling approach with integrated motion compensation," *IEEE Trans. Geosci. Remote Sens.*, vol. 32, no. 5, pp. 1029–1040, Sep. 1994.

[23] G. Fornado, "Trajectory deviations in airborne SAR: Analysis and compensation," *IEEE Trans. Aerosp. Electron. Syst.*, vol. 35, no. 3, pp. 997–1009, Jul. 1999.

[24] P. Prats, K. A. C. D. Macedo, A. Reigber, R. Scheiber, and J. J. Mallorqui, "Comparison of topography- and aperture-dependent motion compensation algorithms for airborne SAR," *IEEE Geosci. Remote Sens. Lett.*, vol. 4, no. 3, pp. 349–353, Jul. 2007.

[25] K. A. C. D. Macedo and R. Scheiber, "Precise topography- and aperture-dependent motion compensation for airborne SAR," *IEEE Geosci. Remote Sens. Lett.*, vol. 2, no. 2, pp. 172–176, Apr. 2005.

[26] S. Perna, V. Zamparelli, A. Pauciullo, and G. Fornaro, "Azimuth-to-frequency mapping in airborne SAR data corrupted by uncompensated motion errors," *IEEE Geosci. Remote Sens. Lett.*, vol. 10, no. 6, pp. 1493–1497, Nov. 2013.

[27] G. Fornaro, G. Franceschetti, and S. Perna, "On center-beam approximation in SAR motion compensation," *IEEE Geosci. Remote Sens. Lett.*, vol. 3, no. 2, pp. 276–280, Apr. 2006.

[28] G. Fornaro, E. Sansosti, R. Lanari, and M. Tesauro, "Role of processing geometry in SAR raw data focusing," *IEEE Trans. Aerosp. Electron. Syst.*, vol. 38, no. 2, pp. 441–454, Apr. 2002.

[29] O. Frey, C. Magnard, M. Ruegg, and E. Meier, "Focusing of airborne synthetic aperture radar data from highly nonlinear flight tracks," *IEEE Trans. Geosci. Remote Sens.*, vol. 47, no. 6, pp. 1844–1858, Jun. 2009.

[30] P. Berardino, C. Esposito, A. Natale, R. Lanari, and S. Perna, "Airborne SAR focusing in the presence of severe squint variations," in *Proc. IEEE Int. Geosci. Remote Sens. Symp. (IGARSS)*, Yokohama, Japan, Jul./Aug. 2019, pp. 537–540.

[31] A. Meta, P. Hoogeboom, and L. P. Ligthart, "Signal processing for FMCW SAR," *IEEE Trans. Geosci. Remote Sens.*, vol. 45, no. 11, pp. 3519–3532, Nov. 2007.

[32] M. Soumekh, *Synthetic Aperture Radar Signal Processing With MATLAB Algorithms*. Hoboken, NJ, USA: Wiley, 1999.

[33] A. F. Yegulalp, "Fast backprojection algorithm for synthetic aperture radar," in *Proc. IEEE Radar Conf. Radar Next Millennium*, Apr. 1999, pp. 60–65.

[34] L. M. H. Ulander, H. Hellsten, and G. Stenstrom, "Synthetic-aperture radar processing using fast factorized back-projection," *IEEE Trans. Aerosp. Electron. Syst.*, vol. 39, no. 3, pp. 760–776, Jul. 2003.

[35] G. Fornaro, G. Franceschetti, and S. Perna, "Motion compensation of squinted airborne SAR raw data: Role of processing geometry," in *Proc. IEEE Int. IEEE Int. Geosci. Remote Sens. Symp. (IGARSS)*, vol. 2, Anchorage, AK, USA, Sep. 2004, pp. 1518–1521.

[36] A. Nemirovski and D. Yudin, *Problem Complexity and Method Efficiency in Optimization*. Hoboken, NJ, USA: Wiley, 1983.

[37] C. Esposito, A. Gifuni, and S. Perna, "Measurement of the antenna phase center position in anechoic chamber," *IEEE Antennas Wireless Propag. Lett.*, vol. 17, no. 12, pp. 2183–2187, Dec. 2018.

[38] M. Jäger, R. Scheiber, and A. Reigber, "External calibration of antenna pointing and positions in airborne SAR systems," in *Proc. 16th Eur. Radar Conf. (EuRAD)*, Oct. 2019, pp. 41–44.

Paolo Berardino was born in Avellino, Italy, in 1971. He received the Laurea degree in nautical sciences from Naval Institute University, Naples, Italy, in 1998. His thesis focused on Synthetic Aperture Radar (SAR) Geocoding.

He joined the Istituto per il Rilevamento Elettromagnetico dell'Ambiente (IREA, formerly IRECE), Institute of the Italian National Research Council (CNR), Naples, in 1999, where he is currently a Researcher. He is interested in the development of algorithms for geocoding of SAR images and studies of surface deformation by using differential SAR interferometry (DInSAR). He has collaborated in the development of a new approach for the analysis of the temporal evolution of the deformation of the Earth's surface based on the combination of differential interferograms (small baseline subset, briefly, SBAS, technique). Over the years, he has participated actively in the upgrading of the SBAS technique: high resolution, geometric registration, data integration European Remote Sensing (ERS) / Environmental Satellite (ENVISAT), and geographic information system (GIS) integration. He has participated in several studies of volcanic areas (Etna, Campi Flegrei, Vesuvius, and Tenerife), seismogenic (central Apennines, Greece), landslide areas (Maratea), and urban areas (Naples and Los Angeles) using the technique SBAS and collaborating with different national (Vesuvius Observatory, Istituto Nazionale di Geofisica e Vulcanologia, briefly, INGV, and Istituto di Ricerca per la Protezione Idrogeologica, briefly, IRPI) and international (Jet Propulsion Laboratory, briefly, JPL, Universidad Complutense de Madrid, briefly, UCM) scientific institutions. His work is currently focused on the development of airborne SAR interferometry techniques, in particular, on algorithms for the elaboration of data acquired from nonlinear flight tracks.

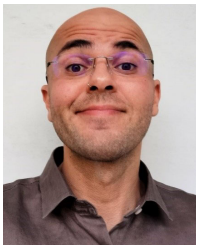

Antonio Natale received the M.S. degree (cum laude) in telecommunication engineering and the Ph.D. degree in electronic and telecommunication engineering from the University of Naples Federico II, Naples, Italy, in 2008 and 2012, respectively.

In 2011, he was a Visiting Scholar with the Surrey Space Centre, University of Surrey, Guildford, U.K., to investigate the application capabilities of NovaSAR-S. In 2013, he spent a period as a Visiting Scientist with the NATO Centre for Maritime Research and Experimentation, La Spezia, Italy, to develop target detection and tracking strategies from high-resolution radar data. In 2022, he was a Visiting Scientist with the National University of Cuyo, Mendoza, Argentina, to devise processing approaches for polarimetric SAOCOM data. Since 2012, he has been with the Institute for Electromagnetic Sensing of the Environment of the National Research Council (IREA-CNR), Naples, where he currently holds the position of researcher. His research interests include remote sensing, with special regard to the modeling of electromagnetic scattering from natural surfaces, signal processing, and the estimation of parameters from radar data. In particular, he is currently involved in developing processing strategies for airborne synthetic aperture radar (SAR) data acquired with strong motion errors.

Dr. Natale was a recipient of the 2009 S.A. Schelkunoff Transactions Prize Paper Award by the IEEE Antennas and Propagation Society, for the best paper published in 2008 on the IEEE TRANSACTIONS ON ANTENNAS AND PROPAGATION. He serves as a Reviewer for international journals on *Remote Sensing* and *Signal Processing*.

Carmen Esposito received the master's degree (summa cum laude) in telecommunication engineering from the Università degli Studi di Napoli "Parthenope," Naples, Italy, in 2012, and the Ph.D. degree in information engineering from the Università degli Studi del Sannio, Benevento, Italy, in 2016.

Since 2012, she has been with the Istituto per il Rilevamento Elettromagnetico dell'Ambiente (IREA), Institute of the Italian National Research Council (CNR), Naples, where she is currently a Researcher. Her main research activities are focused on the processing of airborne synthetic aperture radar (SAR) data with particular emphasis on advanced SAR interferometry techniques and the performance analysis of new-borne radar systems.

Riccardo Lanari (Fellow, IEEE) received the Laurea degree (summa cum laude) in electronic engineering from the University of Naples Federico II, Naples, Italy, in 1989.

In 1989, he joined IRECE and after that Institute for Electromagnetic Sensing of the Environment (IREA), both Research Institutes of the Italian Council of Research (CNR), Naples. From December 2010 to September 2021, he was the Director of IREA where he currently holds the position of research director. He has more than 30 years of research experience in the remote sensing field, particularly on space-borne and air-borne synthetic aperture radar (SAR) and SAR interferometry (InSAR) data-processing methods developments, and their applications in the geosciences. On these topics, he is the holder of two patents and he has coauthored the book *Synthetic Aperture Radar Processing* (CRC Press, 1999) and 490 scientific publications (145 in ISI journals) that have, nowadays, nearly 18 000 citations (H-index = 63, source: Google Scholar). He was a Visiting Scientist in different foreign research institutes, including the German Aerospace Research Establishment (DLR), Oberphaffenhofen, Germany, in 1991 and 1994; the Institute of Space and Astronautical Science (ISAS), Kanagawa, Japan, in 1993; and the Jet Propulsion Laboratory (JPL), Pasadena, CA, USA, in 1997, 2004, and 2008. He was an Adjunct Professor with the University of Sannio, Benevento, Italy, from 2000 to 2003, and from 2000 to 2008, he was a main Lecturer with the Institute of Geomatics, Barcelona, Spain. Moreover, he has achieved the national scientific habilitation as a Full Professor of telecommunications in December 2013 and as a Full Professor of geophysics in February 2014.

Dr. Lanari was a member of the National Commission for the Prevision and Prevention of Big Risks (Commissione Nazionale Grandi Rischi) from 2017 to 2023. Moreover, he has been an expert of the Italian delegation of the Copernicus Program (for the Spatial Program Committee), since 2022; he has been a member of the Advisory Groups of the Sentinel-1 Next Generation mission, since 2020; the ROSE-L mission, since 2020, the COSMO-SkyMed missions of first generation, from 2015 to 2019, and second generation, since 2020. He received from NASA a recognition in 1999 and a group award in 2001 for his activities related to the SRTM mission. He received the Dorso Prize in 2015, for the Special Section "Research," held under the patronage of the Senate of the Italian Republic. Moreover, he has received the Christiaan Huygens Medal from the European Geosciences Union (EGU) in 2017 and the Fawwaz Ulaby Distinguished Achievement Award from the IEEE Geoscience and Remote Sensing Society (GRSS) in 2020. Since 2001, he has been a Distinguished Speaker of the Geoscience and Remote Sensing Society of the IEEE and he has lectured in several national and foreign universities and research centers and served as a Chairperson/Convener and/or a Scientific Program Committee Member at many international conferences.

Stefano Perna (Senior Member, IEEE) received the Laurea degree (summa cum laude) in telecommunication engineering and the Ph.D. degree in electronic and telecommunication engineering from the Università degli Studi di Napoli "Federico II," Naples, Italy, in 2001 and 2006, respectively.

Since 2006, he has been with the Dipartimento di Ingegneria (DI), Università degli Studi di Napoli "Parthenope," Naples, where he is currently a Professor of electromagnetic fields. He currently holds also the position of adjunct researcher with the Institute for Electromagnetic Sensing of the Environment of the National Research Council (IREA-CNR), Naples. Since 2015, he has been collaborating with the Argentinian National Council of Technical and Scientific Research (CONICET) on activities relevant to the focusing and processing of airborne synthetic aperture radar (SAR) data. In 2016, he was a Visiting Professor with the Departamento de Teoría de la Señal y Comunicaciones, Universitat Politècnica de Catalunya (UPC), Barcelona, Spain. He is responsible for several research projects relevant to the realization and testing of novel radar systems, and the focusing and processing of airborne SAR data. Since 2020, he has been a member of the Mission Advisory Group (MAG) of the PLATINO-1 SAR mission funded by the Italian Space Agency (ASI). His main research interests are in the field of microwave remote sensing and electromagnetics: airborne SAR data modeling and processing, airborne differential SAR interferometry, modeling of electromagnetic scattering from natural surfaces, synthesis of antenna arrays, antenna characterization, and measurement in anechoic and reverberating chambers.